C O M M O N S D E E D

저작자표시-비영리-변경금지 2.0 대한민국

이용자는 아래의 조건을 따르는 경우에 한하여 자유롭게

- 이 저작물을 복제, 배포, 전송, 전시, 공연 및 방송할 수 있습니다.

다음과 같은 조건을 따라야 합니다:

저작자표시. 귀하는 원저작자를 표시하여야 합니다.

비영리. 귀하는 이 저작물을 영리 목적으로 이용할 수 없습니다.

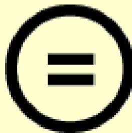

변경금지. 귀하는 이 저작물을 개작, 변형 또는 가공할 수 없습니다.

- 귀하는, 이 저작물의 재이용이나 배포의 경우, 이 저작물에 적용된 이용허락조건을 명확하게 나타내어야 합니다.
- 저작권자로부터 별도의 허가를 받으면 이러한 조건들은 적용되지 않습니다.

저작권법에 따른 이용자의 권리는 위의 내용에 의하여 영향을 받지 않습니다.

이것은 이용허락규약(Legal Code)을 이해하기 쉽게 요약한 것입니다.

Disclaimer

dCollection

Formation of Epitaxial Graphene Layers on 6H-SiC Induced by Electron Beam Irradiation

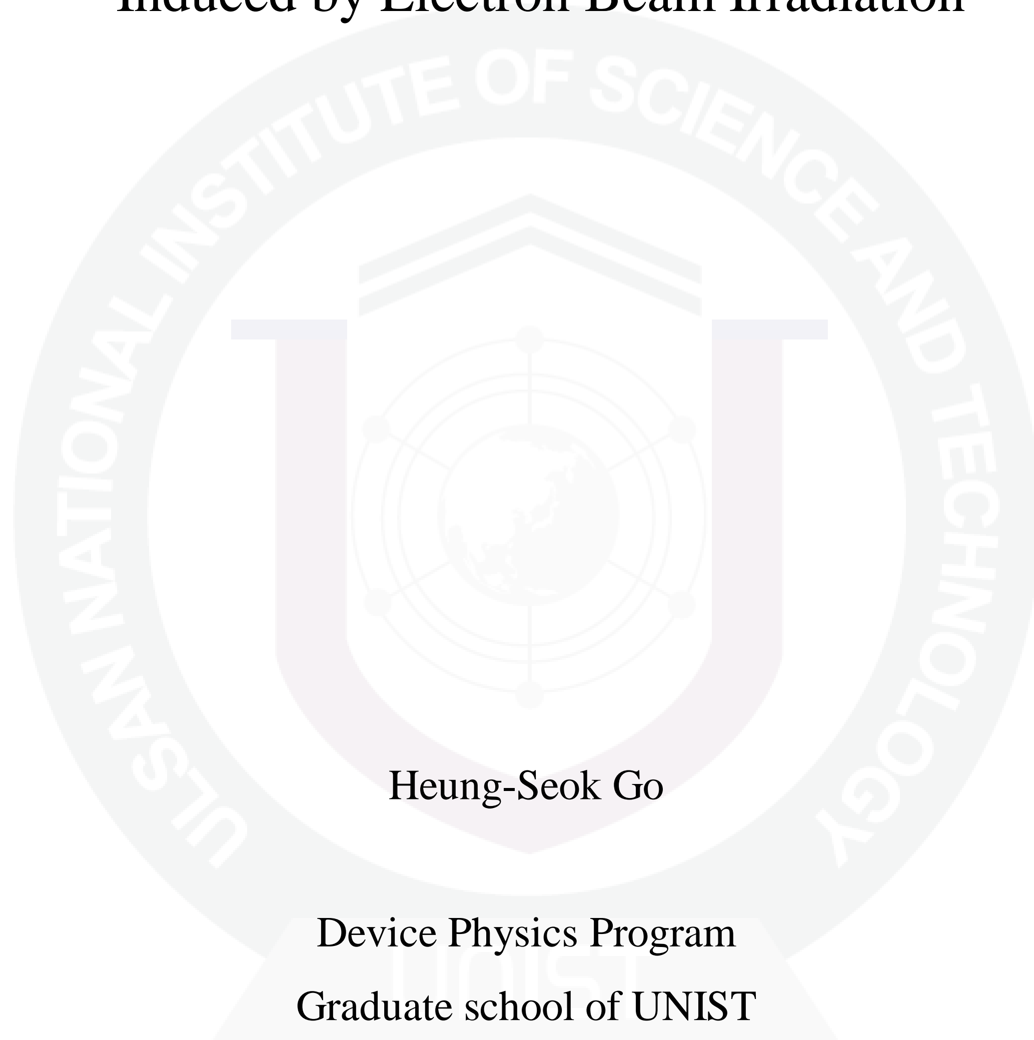

Heung-Seok Go

Device Physics Program

Graduate school of UNIST

2012

Formation of Epitaxial Graphene Layers on 6H-SiC Induced by Electron Beam Irradiation

Heung-Seok Go

Device Physics Program

Graduate school of UNIST

Formation of Epitaxial Graphene Layers on 6H-SiC Induced by Electron Beam Irradiation

A thesis
submitted to the Graduate School of UNIST
in partial fulfillment of the
requirements for the degree of
Master of Science

Heung-Seok Go

06. 04. 2012
Approved by

____

Major Advisor
Kibog Park

Formation of Epitaxial Graphene Layers on 6H-SiC Induced by Electron Beam Irradiation

Heung-Seok Go

This certifies that the thesis of Heung-Seok Go is approved.

06. 04. 2012

____
Thesis Supervisor: Kibog Park

____
Min Sup Hur: Thesis Committee Member #1

____
Kyung Rok Kim: Thesis Committee Member #2

Abstract

It is observed that the epitaxial graphene layers form on the surface of a 6H-SiC substrate by electron beam irradiation. The electron beam (e-beam) is irradiated by using a commercial electron beam evaporator with acceleration voltage 8kV in high vacuum environment. Raman spectrum measurements show all relevant peaks (D, G, 2D) clearly, confirming the formation of graphene layers. The structural analysis is confirmed by using TEM (Transmission Electron Microscopy). The result of formed graphene layers thickness measurement is verified 7 ~ 8 layers of graphene. It is checked out that thickness of 1 layer is approximately 0.32 nm. The elemental composition of the epitaxial graphene layer is measured with AES (Auger Electron Spectroscopy) and XPS (X-ray Photoelectron Spectroscopy). The sheet resistance of the epitaxial graphene layer which is measured by forming CTLM (Circular Transmission Line Model) patterns on the irradiated 6H-SiC surface is found to decrease at least 1000 times, compared with the original 6H-SiC substrate. The sheet resistance and contact resistance of graphene layer are 6.7 kΩ/□ and 0.18 kΩ respectively. Also, the quality of the graphene layer in terms of Raman spectrum and sheet resistance is found to be improved noticeably as the electron fluence (e/cm^2) is increased by making the irradiation time longer.

Contents

I. Introduction 1

1.1 Silicon Carbide 1

1.1.1 Theoretical Background 1

1.1.2 Structure of Silicon Carbide 4

1.1.3 Major SiC Polytypes 6

1.1.4 Properties of Silicon Carbide 9

1.2 Graphene 12

1.2.1 Definition & Application 12

1.2.2 Properties of Graphene 15

1.2.3 Process Methods 17

1.3 Graphene on Silicon Carbide 19

II. Approaches & Measurement 21

2.1 Experiment Method 21

2.2 Research Results 24

2.2.1 Structural and Compositional Analysis 24

2.2.1.1 Raman Spectrum Analysis 24

2.2.1.2 Transmission Electron Microscopy Analysis 29

2.2.1.3 Auger Electron Spectroscopy Analysis 33

2.2.1.4 X-ray Photoelectron Spectroscopy Analysis 38

2.2.2 Electrical Characteristics 41

2.2.2.1 Two-Terminal Resistance Measurement 41

2.2.2.2 Circular Transmission Line Model 43

III. Summary & Conclusion 49

List of Figures

Figure 1-1 Applications of SiC material.

Figure 1-2 Structure of SiC.

Figure 1-3 Structure of major SiC polytypes.

Figure 1-4 Applications of graphene.

Figure 1-5 Methods of graphene growth.

Figure 1-6 Schematic diagrams showing the formation of epitaxial graphene on 6H-SiC substrate.

Figure 2-1 Appearance and inner structure of e-beam evaporator.

Figure 2-2 Image and temperature of e-beam irradiation.

Figure 2-3 Raman shifts of graphene layers.

Figure 2-4 I_D/I_G & I_{2D}/I_G ration & 2D peak Lorentzian fitted data of graphene layers.

Figure 2-5 Measurement of graphene's thickness by using TEM.

Figure 2-6 AES spectra of 6H-SiC and graphene layer (Differentiated & Undifferentiated Mode).

Figure 2-7 AES spectra – C range (Differentiated & Undifferentiated Mode).

Figure 2-8 AES spectra – O range (Differentiated & Undifferentiated Mode).

Figure 2-9 AES spectra – Si range (Differentiated & Undifferentiated Mode).

Figure 2-10 XPS spectra of 6H-SiC and graphene layers formed by e-beam irradiation (2 hr).

Figure 2-11 Image of dot metal contacts.

Figure 2-12 The current-voltage characteristics of graphene layers formed by e-beam irradiation.

Figure 2-13 CTLM image for metal contact.

Figure 2-14 Cross-section image of CTLM.

Figure 2-15 Pattern of CTLM.

Figure 2-16 Graph of R_T versus d.

Figure 2-17 R_T versus d curve of CTLM.

Figure 2-18 Current-voltage curve of CTLM.

List of Tables

Table 1-1 Properties of major SiC polytypes.

Table 1-2 Parameter of e-beam irradiation.

Table 2-2 XPS elements and quantifications of 6H-SiC and graphene layers form by e-beam irradiation (2 hr).

Nomenclature

SiC Silicon Carbide.

LED Light Emitting Diode.

MOSFET Metal Oxide Semiconductor Field Effect Transistor.

BCC Body Centered Cubic.

FCC Face Centered Cubic.

ZnS Zinc Sulfide.

ITO Indium Tin Oxide.

PVD Physical Vapor Deposition.

CVD Chemical Vapor Deposition.

MEMS Micro Electro Mechanical Systems.

PR Photo Resist.

FWHM Full Width Half Maximum.

RT Room Temperature.

TEM Transmission Electron Microscopy.

AES Auger Electron Spectroscopy.

SAM Scanning Auger Microscopy.

SIMS Secondary Ion Mass Spectrometry.

FFA Face Field Analyzer.

XPS X-ray Photoelectron Spectroscopy.

UHV Ultra High Vacuum.

RSF Relative Sensitivity Factor.

AFM Atomic Force Microscopy.

ML Monolayer.

BL Bilayer.

TL Trilayer.

SEM Scanning Electron Microscope.

STM Scanning Tunneling Microscope.

TLM Transmission Line Model.

CTLM Circular Transmission Line Model.

Chapter I

Introduction

Silicon Carbide (SiC) is a compound of silicon and carbon with chemical formula SiC. SiC is a wide gap semiconductor material with excellent electronic and physical properties such as high electron draft velocity, high breakdown field and high thermal conductivity. These properties make SiC promising for certain extreme applications including high voltage, high power and high temperature devices.

Graphene is an allotrope of carbon. Its structure is one-atom-thick planar sheets of sp^2-bonded carbon atoms that are densely packed in a honeycomb crystal lattice. It is a promising electronic material for future nano-electronics, due to its high carrier mobility and high Fermi velocity compared to conventional semiconductors.

This chapter demonstrates that formation of graphene layers on the SiC surface by using electron beam (e-beam) irradiation. And it will be introduced structural, compositional and electrical analysis of formed graphene layers on the SiC substrate.

1.1. Silicon Carbide

SiC materials are used in a variety of ways. Its powder has been mass-produced since 1893 for use as an abrasive. Grains of SiC can be bonded together by sintering to form very hard ceramics which are widely used in applications requiring high durability, such as car brakes, clutches and ceramic plates in bulletproof vests. Electronic applications of SiC as light emitting diodes (LEDs) and detectors were first demonstrated around 1907, and today it is widely used in high-temperature, high-voltage semiconductor electronics. It already plays an important role in the modern electronics industry. It is available at the moment from different suppliers has been considerably improved over the last years.

1.1.1. Theoretical Background

SiC is the only chemical compound of carbon and silicon. It was originally produced by a high temperature electro-chemical reaction of sand and carbon. It is an excellent abrasive and has been produced and made into grinding wheels and other abrasive products for over one hundred years. Today it has been developed into a high quality technical grade ceramic with very good mechanical properties. It is used in grinding wheel, seal ring, ballistic vest, ceramics, and numerous high-

performance applications. It can also be applied for electrical devices such as, power MOS-FET and LED. And it is used as semiconductor equipment components. There are heating elements and susceptor and so on [Fig. 1-1].

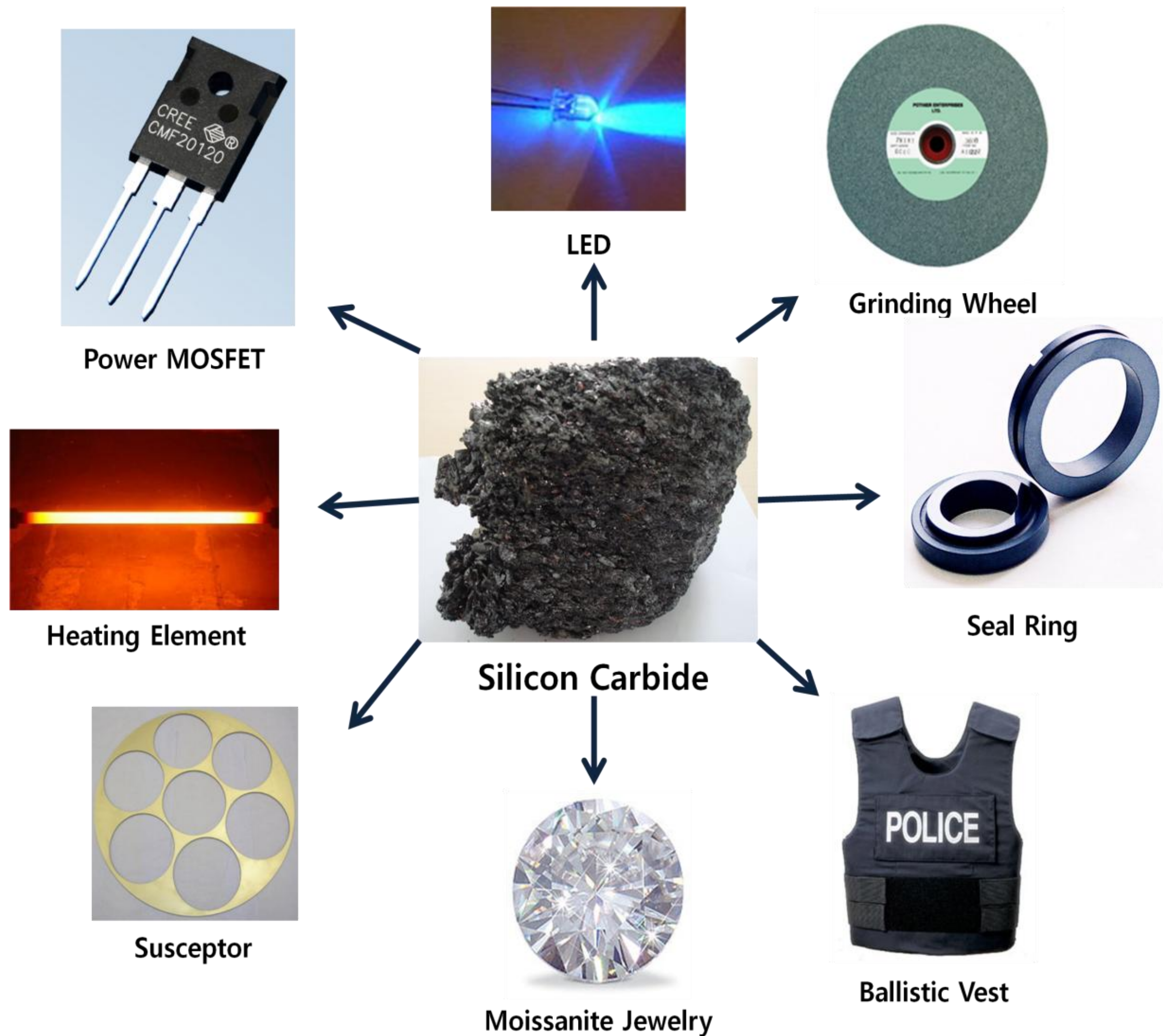

Figure 1-1: Applications of SiC material

Jons Jacob Berzelius, who is mostly known for his discovery of Si, was the first person who synthesized SiC. In 1824, he published a paper in which he assumed that there was a chemical bond between Silicon and Carbon [1][2]. A few years later, Acheson produced suitable minerals that could substitute diamond as an abrasive and cutting material. He mixed coke and silica in a furnace and found a crystalline product characterized by a great hardness, refractability, and infusibility, which was shown to be a compound of Silicon and Carbon. Acheson called his product ‘carborundum’ and name it the proper formula: SiC. Moissan found the first natural SiC crystal in a meteorite in 1905. That is why mineralogists call natural SiC moissanite. In 1907, H.J. Round produced the first Light Emitting Diode (LED) by applying voltage on contacts of SiC crystal, observing yellow, green and

orange luminescence at the substrate. Five years later, Baumhauer used the word ‘poly-type’ to describe the ability of SiC to crystallise into different forms varying only in their stacking order in one direction. As semiconductor material, several attempts were considered. In 1955, Lely presented a new concept of growing high quality SiC crystals. Lely created a mini-environment for the growth of crystals similar to the growth in the voids in the Acheson process. This created renewed interest in SiC as a semiconductor material and, at that time, SiC was even more popular than Si and Ge. This would soon change, as we all know, mainly due to the difficulty in obtaining high-purity SiC wafers. In 1978, Tairov and Tsvetkov made a discovery of comparable dimension and importance to the Acheson process. They managed to produce SiC high purity substrates by seeded sublimation growth. The SiC wafer was born. Two years later was the ability to grow epitaxial SiC on Si substrates. In 1987, high-quality epitaxy was performed at low temperatures on off-axis substrates. Cree Inc. was founded in 1989. This company manufactured the first commercial blue SiC LED and began to sell SiC wafers. In the same time, Cree produced demonstrators for power devices and high frequency devices. Along with better epitaxy, continuous improvement of the diameter and quality of the wafers, and device evolution is still under way. The future for SiC looks very bright now that commercial products have hit the marketplace.

SiC has been used in the electronic fields extensively. Especially, there are remarkable in the power electronic devices and LED fields. It is used for ultrafast, high-voltage Schottky diodes, MOSFETs and high-temperature thyristors for high-power switching [3][4]. As a material, its uses were initially limited to grinding and polishing. But material quality, size, and cost have significantly improved over just the last several years to make it a realizable replacement for Silicon in power devices. Commercial uses of SiC have happened over just the last few years. The limiting factor as with all new techniques has been cost. Cree has been utilizing SiC as a semiconductor material in the production of devices and LEDs. The defect density has been reduced to a low enough level to allow the fabrication of large area power devices with an acceptable yield. With wafer size going up and defect densities going down, the possible device size is growing rapidly. Simultaneously, material costs are dropping and a true competition with Silicon. SiC has several unique properties that lend themselves to the development of high voltage devices. SiC has a strong advantage over Si and GaAs. The thermal conductivity of SiC is several times that of GaAs and over three times that of Si. In fact, at room temperature, 4H-SiC has a higher thermal conductivity than Copper. The higher breakdown field of SiC is almost nine times the breakdown field of Si. The bandgap is defined as the energy difference between the valence band and the conduction band in the material. In wide bandgap materials (like SiC), the thermal generation of current flow is much small than in Si. This leads to the ability to operate at much higher temperatures than Si counterparts with lower leakage current.

SiC is composed of tetrahedron of Silicon and Carbon atoms with strong bonds in the crystal lattice. This produces a very hard and strong material. In air, it forms a protective silicon oxide coating at 1200℃ and is able to be used up to 1600℃. The high thermal conductivity coupled with low thermal expansion and high strength give this material exceptional thermal shock resistant qualities. SiC ceramics with little or no grain boundary impurities maintain their strength to very high temperatures, approaching 1600℃ with no strength loss. Chemical purity, resistance to chemical attack at temperature, and strength retention at high temperatures has made this material very popular as wafer tray supports and paddles in semiconductor furnaces. The electrical conduction of the material has lead to its use in resistance heating elements for electric furnaces, and as a key component in thermistors (temperature variable resistors) and in varistors (voltage variable resistors).

The history of SiC LEDs is quite remarkable. SiC has been widely used as material for manufacturing yellow, red, green LED and optical devices [5]. The SiC LED technology has been investigated for improvement of their operational characteristics. The first LED application was demonstrated in 1907 using SiC and the first commercial LEDs were again based on SiC. Yellow LEDs made from 3C-SiC were manufactured in the Soviet Union in the 1970s. and blue ones (6H-SiC) worldwide in the 1980s. SiC LED first became a significant commercial success when CREE got them on the market in the early 1990s. CREE's CB series of super bright LED are a new generation of solid-state LED emitters, which combine highly efficient InGaN with Cree's SiC substrate. Cree's main LED products now have SiC as a substrate for GaN or InGaN as active ingredients, and emit blue as well as green and blue-green luminescence. SiC is one of the important LED components. It is a popular substrate for growing GaN devices, and it also serves as a heat spreader in high-power LEDs.

1.1.2. Structure of Silicon Carbide

Many compound materials present polymorphism, that is they can exist in different structures called polymorphs. SiC is unique in this regard as more than 250 polymorphs of silicon carbide had been identified. Some of them having a lattice constant as long as 301.5 nm, about one thousand times the usual SiC lattice spacings.

The polymorphs of SiC include various amorphous phases observed in thin films and fibers, as well as a large family of similar crystalline structures called polytypes [6][7]. They are transitions of the same chemical compound that are equivalent in two dimensions and differ in the third. Thus, they can be showed as layers stacked in a certain sequence. The atoms of those layers can be arranged in three configurations, A, B or C to achieve closest packing. The stacking sequence of those

compositions defines the crystal structure, where the unit cell is the shortest periodically repeated sequence of the stacking sequence. This depiction is not unique to SiC, but also applies to other binary tetrahedral materials, such as Zinc Oxide and Cadmium Sulfide. The polymorphism of SiC is characterized by a large family of similar crystalline structures called polytypes. They are variations of the same chemical compound that are identical in two dimensions and differ in the third. Thus, they can be viewed as layers stacked in a certain sequence. Alpha silicon carbide (α-SiC) is the most commonly presented polymorph [Fig. 1-2]. It is built at temperatures greater than 1700 ℃ and has a hexagonal crystal structure (similar to Wurtzite). The beta transformation (β-SiC), with a zinc blende crystal structure (similar to Diamond), is formed at temperatures below 1700 ℃ [7][8]. Until recently, the beta form has had relatively few commercial uses, although there is now increasing interest in its use as a support for heterogeneous catalysts, owing to its higher surface area compared to the alpha form. The high sublimation temperature of SiC makes it useful for bearings and furnace parts at approximately 2700 ℃. It does not melt at any known pressure. It is also highly inert chemically. There is currently much interest in its use as a semiconductor material in electronics, where its high thermal conductivity, high electric field breakdown strength and high maximum current density make it more promising than silicon for high powered devices. It also has a very low coefficient of thermal expansion and experiences no phase transitions that would cause discontinuities in thermal expansion [9][10].

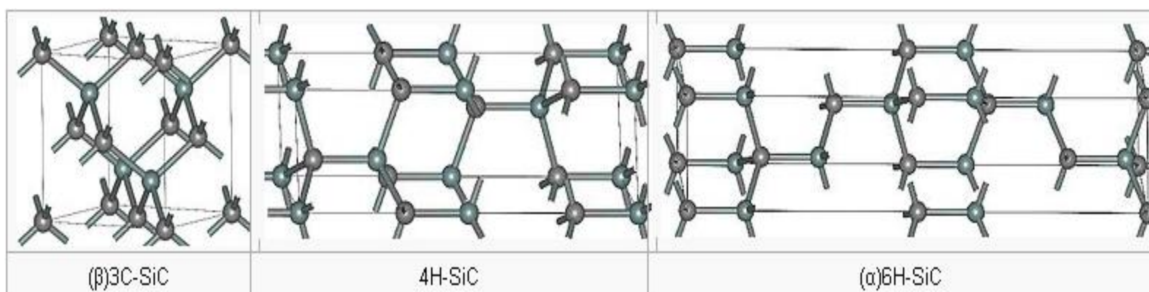

Figure 1-2: Structure of SiC

1.1.3. Major SiC Polytypes

SiC is the hybridization of silicon and carbon atoms. Both silicon and carbon atoms have sp^3 hybrid orbits, which form tetrahedrals bonding by taking combination of atomic orbitals of other atoms. The Si-C bonds in SiC are formed by overlapping each sp^3 hybrid orbital of carbon atom with a corresponding orbital of four neighboring silicon atoms.

Polytypes of typically commercialized SiC are 3C-SiC, 4H-SiC and 6H-SiC [11][12]. The 3C-SiC polytype is with 3 stacking layers, ABC/ABC…, and with cubic crystal structure. There are 4H-SiC polytype with 4 stacking layers, ABCB/ABCB…, and with hexagonal crystal structure and 6H-SiC polytype with 6 stacking layers, ABCACB/ABCACB…, and with hexagonal crystal structure [Fig. 1-3]. SiC is in fact the material in which polytypism was first discovered and more than 250 polytypes of SiC have been reported up to now. In the case of SiC, the basis is the Si-C bilayer with silicon and carbon atoms separated by 1.89 Å. The Si-C pairs in one bilayer (basal plane) form the hexagonal close-packed structure. The crystal structure of SiC is actually found to be three-dimensional close-packing. In this case, there are two same ways to stack one hexagonal basal plane on top of another one. Suppose that the Si-C pairs in the first basal plane occupy the locations depicted as ‘A’ in [Fig. 1-2] where Si atom is drawn to be larger than C atom since Si-C bond is expected to be more covalent. Then, in the second basal plane, they can occupy either ‘B’ or ‘C’ positions to be close-packed along the stacking direction. If ‘B’ positions are here occupied, then Si-C pairs in the third basal plane can occupy either ‘A’ or ‘C’ position. Accordingly, by stacking Si-C bilayers continuously by following this rule, it is possible to have an infinite number of different stacking sequences of basal planes, each resulting in a different crystal structure. In this type of three-dimensional close-packed structure, a Si atom is bonded to the nearest four C atoms tetrahedrally and in reverse.

One case in the basal plane (Si-C bilayer) stacking is the one where the stacking sequence is ABC/ABC in the classical ABC notational system. The triangle in stacking sequence shown in the figure represent the projection of the tetrahedron composed of one Si atom and four nearest-neighbor C atoms on the plane. The central Si atom and two C atoms are in fact in the plane. The other two C atoms are located away from the plane on both sides by the half of the smallest lattice vector in the hexagonal basal plane and the black closed circle depicted with a shorter bond (solid black line) length to the Si atom represent the projection of these two C atoms on the plane. The crystal structure with this ABC stacking sequence is found to be pure cubic, in other words, a zinc-blende structure consisting of two interpenetrating face-centered cubic (fcc) lattices. This polytype is usually named 3C following the Ramsdell notation where the front number represent the number of layers in the unit cell and the following letter specifies the lattice type. The C signify ‘cubic’ and the H is ‘hexagonal’. It is sometimes called β-SiC because of its similarity with β-ZnS (zinc sulfide) that originated the

name of ‘zinc-blende’. This 3C polytype can also be denoted as in the Hägg notation describing a polytype by specifying the relationship between successive layers, i.e., cyclic stackings (AB, BC, and CA) denoted with the sign and anticyclic stackings (AC, CB, and BA) with the sign. The unit cell of 3C-SiC is shown with the distribution of the Si and C atoms inside it in [Fig. 1-3]. The stacking direction of the basal planes perpendicular to the planes is in fact [111] direction of the cubic unit cell of 3C-SiC as indicated in the figure [13].

Another extreme case in the stacking is when the stacking sequence is AB/AB illustrated in [Fig. 1-2], inducing a pure hexagonal wurtzite structure. This polytype is labeled 2H in the Ramsdell notation and in the Hägg notation. Its unit cell and the distribution of the base atoms are represented in [Fig. 1-2]. One difference of pure cubic and hexagonal stackings is the relative orientation of the respective bonds of Si and C atoms in a bilayer to C and Si atoms in the adjacent layers. In the cubic stacking, the bonds are staggered when they are seen from the stacking direction while the bonds in the hexagonal stacking are eclipsed. Other polytypes are essentially combinations of the cubic and hexagonal stackings.

The 4H- and 6H-SiC are the most common polytypes, and single crystal wafers of these polytypes are currently available and hence all recent research for making commercial devices out of SiC are focused on these polytypes. The stacking sequence of 4H-SiC is written as ABCB/ABCB and that of 6H-SiC is ABCACB/ABCACB. The corresponding Hägg notations are 4H and 6H respectively. Since the SiC polytypes are mixtures of cubic and hexagonal stackings, a quantity defined as the hexagonality H representing the fraction of hexagonal stackings out of all the stackings (cubic + hexagonal) in a polytype is used frequently to describe how much the polytype is cubic-like or hexagonal-like in structural sense. For instance, 4H-SiC has the hexagonality of 50 % and 6H-SiC has 33%. As is obvious from the definition, the hexagonality of 2H-SiC is 100 % and that of 3C-SiC is 0 %. It is naturally expected that a polytype with a smaller H should be closer to 3C, that is, more cubic-like than one with a larger H in other material properties as well as in structure, and this is generally true for most of the polytypes.

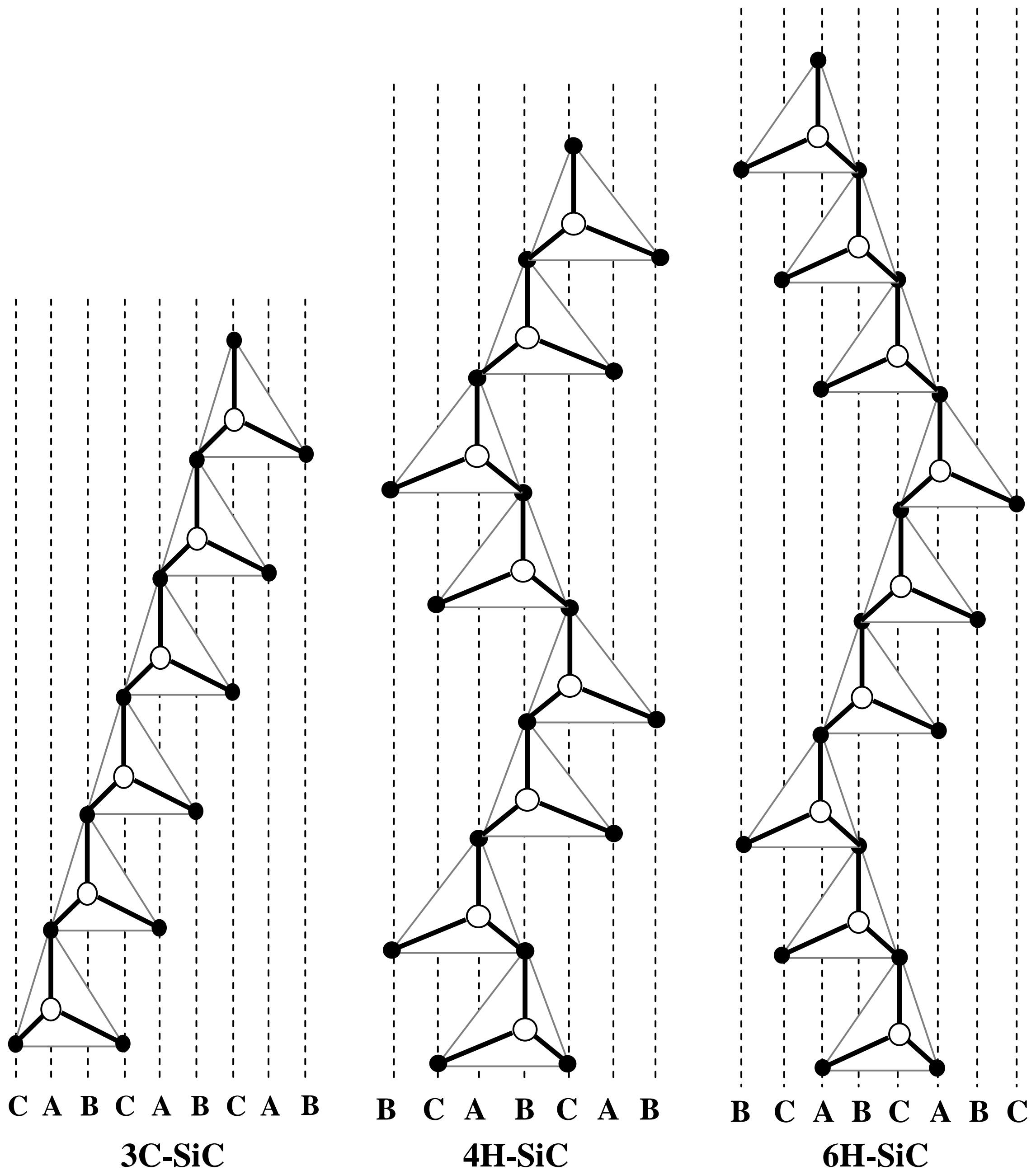

Figure 1-3: Structure of major SiC polytypes

1.1.4. Properties of Silicon Carbide

Pure SiC is colorless. The brown to black color of industrial product results from iron impurities. The rainbow-like luster of the crystals is caused by a passivation layer of silicon dioxide that forms on the surface [14]. The high sublimation temperature of SiC (approximately 2700 ℃) makes it useful for bearings and furnace parts. Silicon carbide does not melt at any known pressure. It is also highly inert chemically. There is currently much interest in its use as a semiconductor material in electronics, where its high thermal conductivity, high electric field breakdown strength and high maximum current density make it more promising than silicon for high-powered devices. SiC also has a very low coefficient of thermal expansion and experiences no phase transitions that would cause discontinuities in thermal expansion. The material characteristics of SiC in structural, mechanical, thermal, and electrical aspects have been described in great detail and compared well with other materials in several references.

The electronic band structures of the SiC polytypes will be mainly discussed since they are the key physical substances together with the polytypism of SiC itself underlying the experimental observations and measurements for the SiC sample systems addressed in this work [15][16]. Those for 4H- and 6H-SiC which are in between the two extreme cases in structure are measured to be 3.265 eV and 3.023 eV respectively. The first-principle calculations of band structures of several polytypes of SiC also have been carried out by many groups. The calculated band gaps in fact vary somewhat considerably depending on the calculation method. For instance, density functional theory with the local density approximation is known to underestimate band gaps. But the overall band structures are very similar from all the calculations. According to the calculations and the experimental supports, the band gaps of SiC polytypes are indirect. This means that the conduction band minimum of each polytype occurs at non-zero crystal momentum, shifted with respect to the valence band maximum that occurs at the Brillouin zone center. The important materials-related problems affecting the performance of all SiC devices and their associated components are the defects and the undesired impurities which become incorporated in the homoepitaxial SiC layers in which all devices are currently fabricated. The reverse blocking leakage current in high voltage Schottky diodes is three orders of magnitude higher than theoretically predicted as a result of defects in the epi-layer. The formation of micro-pipes, stepped screw dislocations, interacting dislocation loops, polyganized networks of dislocations and growth twins as well as stacking faults during the sublimation growth of SiC boules are likely the root cause of some of the defects in the epitaxial layer. However, with the exception of the micro-pipes, the types and concentrations of line, planar and other three-dimensional defects and their effect on the performance of devices and individual device components in the important epi-layer have not been similarly determined. As such, it is not known which of the latter

defects actually are translated from the wafer into the epi-layer during its deposition and, therefore, should be vigorously controlled during boule growth and which defects are generated during deposition. The relatively uncontrolled occurrence of the n-type donor of N and deep level compensating impurities such as Ti in the epilayer have been identified via secondary ion mass spectrometry, photoluminescence and cathodoluminescence investigations. However, the origins of essentially all of these impurities are unknown. For high-temperature, -power and -frequency devices, it is highly desirable to control or eliminate these impurities such as to attain undoped films with uncompensated carrier concentrations of 10^{14} cm^{-3} two orders of magnitude lower than what is, at present, normally achieved in standard commercial depositions. The formation of low resistivity and thermally stable ohmic contacts to 4H- and 6H-SiC remains a serious problem in the development of SiC device technology [17]. For SiC power devices to have an advantage over Si, the contact resistivities must be below 1×10^{-5} W-cm^2, as noted by Alok, et dl. In addition, the electrical characterization of state-of-the-art SiC films depends on the ability to fabricate ohmic contacts on material with low carrier concentrations. Therefore, better ohmic contacts are needed both for improving device performance and for improving the quality of films which can be grown. The thermal stability of ohmic contacts is of particular concern for p-type SiC, which have traditionally relied on low melting point Al or Al alloys to dope the SiC surface below the contacts. These materials are not suitable for devices intended for high-temperature operation. While the fabrication of ohmic contacts to SiC has also normally depended on the attainment of a very heavily-doped near-surface region, the introduction during deposition of high levels of dopants in the near surface device region of the epi-layer prior to the deposition of the contact or by ion implantation through the contact makes probable the introduction of point and line defects as a result of the induced strain in the lattice.

Silicon carbide is a semiconductor, which can be doped n-type by nitrogen or phosphorus and p-type by aluminium, boron, gallium or beryllium. Metallic conductivity has been achieved by heavy doping with boron, aluminium or nitrogen [18]. Superconductivity has been detected in 3C-SiC:Al, 3C-SiC:B and 6H-SiC:B at the same temperature of 1.5 K. A crucial difference is however observed for the magnetic field behavior between aluminium and boron doping. In attempt to explain this difference, it was noted that silicon positions are more important than carbon positions for superconductivity in SiC. Whereas boron substitutes carbon in SiC, Al substitutes Si sites. Therefore, Al and B see different environment that might explain different properties of SiC:Al and SiC:B. There are properties of major SiC polytypes as follows.

Property	3C-SiC	4H-SiC	6H-SiC
Crystal Structure	Zinc blende (cubic)	Hexagonal	Hexagonal
Lattice Constant (Å)	4.3596	3.073	3.073
Density (g/cm^3)	3.21	3.21	3.21
Bandgap (eV) at 300K	2.3	3.3	2.9
Maximum operating Temperature (℃)	873	873	873
Melting poing (℃)	> 1800	> 1800	> 1800
Chemical & Physical Stabilities	Excellent	Excellent	Excellent
Electron Mobility (cm^2/V•s)	1000	900	600
Hole Mobility (cm^2/V•s)	40	100	40
Breakdown field (10^{-6} V/cm)	4	4	4
Thermal Conductivity (W/cm•℃)	5	5	5
Sat. Elect. Drift Velocity (10^7cm/s)	2.5	2.5	2.5
Dielectric Constant	9.7	9.7	9.7

Table 1-1: Properties of major SiC polytypes

1.2. Graphene

Graphene is a flat monolayer of carbon atoms tightly packed into a two-dimensional (2D) honeycomb lattice, and is a basic building block for graphitic materials of all other dimensionalities. It can be wrapped up into 0D fullerenes, rolled into 1D nanotubes or stacked into 3D graphite.

1.2.1. Definition & Application

The graphene is a substance which has a single-layer crystal lattice of carbon atoms, which is unusual since it is different from all of the materials of its kind [19][20]. Several researchers have identified a way of making this substance, which allows them to use it in various fields and especially for the high-speed electronic devices. Graphene is defined as a one atom thin sheet of carbon atoms arranged in a Hexagonal format or a flat monolayer of carbon atoms that are tightly packed into a 2D honeycomb lattice. In October 2010, two University of Manchester (U.K.) scientists, Andre Geim and Konstantin Novolselov, were awarded the 2010 Nobel Prize in physics for their research on graphene. Graphene is a one-atom-thick sheet of carbon whose strength, flexibility, and electrical conductivity have opened up new horizons for high-energy particle physics research and electronic, optical, and energy applications. Graphene oxide, a single-atomic-layered material made by reacting graphite powders with strong oxidizing agents, has the ability to easily convert into graphene a low-cost carbon-based transparent and flexible electronics. Graphene oxide has been known in the scientific world for more than a century and was largely described as hydrophilic, or attracted to water. These graphene oxide sheets behave like surfactants, the chemicals in soap and shampoo that make stains disperse in water. Graphene can be used in various ways [Fig. 1-4].

- Organically doped graphene-based solar cell achieves new efficiency record : Researchers from the University of Florida have managed to develop the most efficient graphene based solar cell to date. This was achieved by doping it with an organic material, and it increases the efficiency by more than for times (from 1.9 % to 8.6 %). The researchers used a cheap and environmentally stable organic coating layer to reduce the graphene electrical resistance by adjusting the Fermi level. In the new solar cells, a single layer of graphene placed on top of a silicon wafer serves as a Schottky junction, the main component of simple photovoltaic devices called Schottky junction solar cells.

- Graphene based anti-corrosion coating shows great promise : The University at Buffalo developed a new graphene-based anti-corrosion coatings. These new coatings are effective and eco-friendly as opposed to currently used hexavalent chromium (which is a potential carcinogen) based coating. Graphene’s conductive and hydrophobic properties are helpful in

preventing corrosion by repelling water and inhibiting electro-chemical reactions. The graphene-based composite can be fine-tuned for use in factories specializing in chrome electroplating.

- Samsung develops a new graphene-based transistor : Samsung’s Advanced Institute of Technology have developed a new graphene-silicon Schottky barrier that enables graphene to switch electric current on and off. The researchers explored potential logic device applications based on this technology.

- Quantum Dots and graphene can create highly sensitive photodetectors : The Institute of Photonic Sciences (ICFO) in Barcelona, Spain have developed a highly sensitive photodetector that uses graphene and quantum dots. They say that the new device is a billion times more sensitive to light than previous graphene-based photodetectors because of the quantum dots. A photodetector such as this can be used in light sensors, solar cells, infrared cameras and biomedical imaging. Graphene’s external quantum efficiency (EQE) is low as it absorbs less than 3% of the light that falls on it. It is also quite difficult to actually extract the electrical current from the graphene. Adding the quantum dots on the graphene sheet helps both of these issues.

- Graphene and Cobalt used to make a spin-controlled material : The University of South Florida and the University of Kentucky managed to create a material the spin of the electrons can be set in a controlled manner. The team suggests using cobalt atoms on a graphene sheet. The researchers have used state-of-the-art theoretical computations to prove this, they haven't actually made the material and controlled the spin.

- Graphene based ITO replacement : The UK's University of Exeter discovered a new graphene based material that can be used as an ITO replacement - it's a lightweight, flexible and transparent conductor. In fact it's more flexible than ITO. To create the new material, the researchers compressed ferric chloride molecules between two sheets of graphene. They are also working on a spray-on version of the material.

- Graphene behaves like a laser when excited with short light pulses : The Iowa State University discovered that graphene behaves like a laser when excited with very short femto second light pulses. Graphene has been shown to have two technologically important properties – population inversion of electrons and optical gain. This means that graphene can be used to make a variety of optoelectronics devices, including broadband optical amplifiers, high-speed modulators, and absorbers for telecommunications and ultra fast lasers.

The properties of graphene, carbon sheets that are only one atom thick, have caused researchers and companies to consider using this material in several fields. It is a rapidly rising star on the horizon of materials science and condensed-matter physics. This strictly two-dimensional material exhibits exceptionally high crystal and electronic quality.

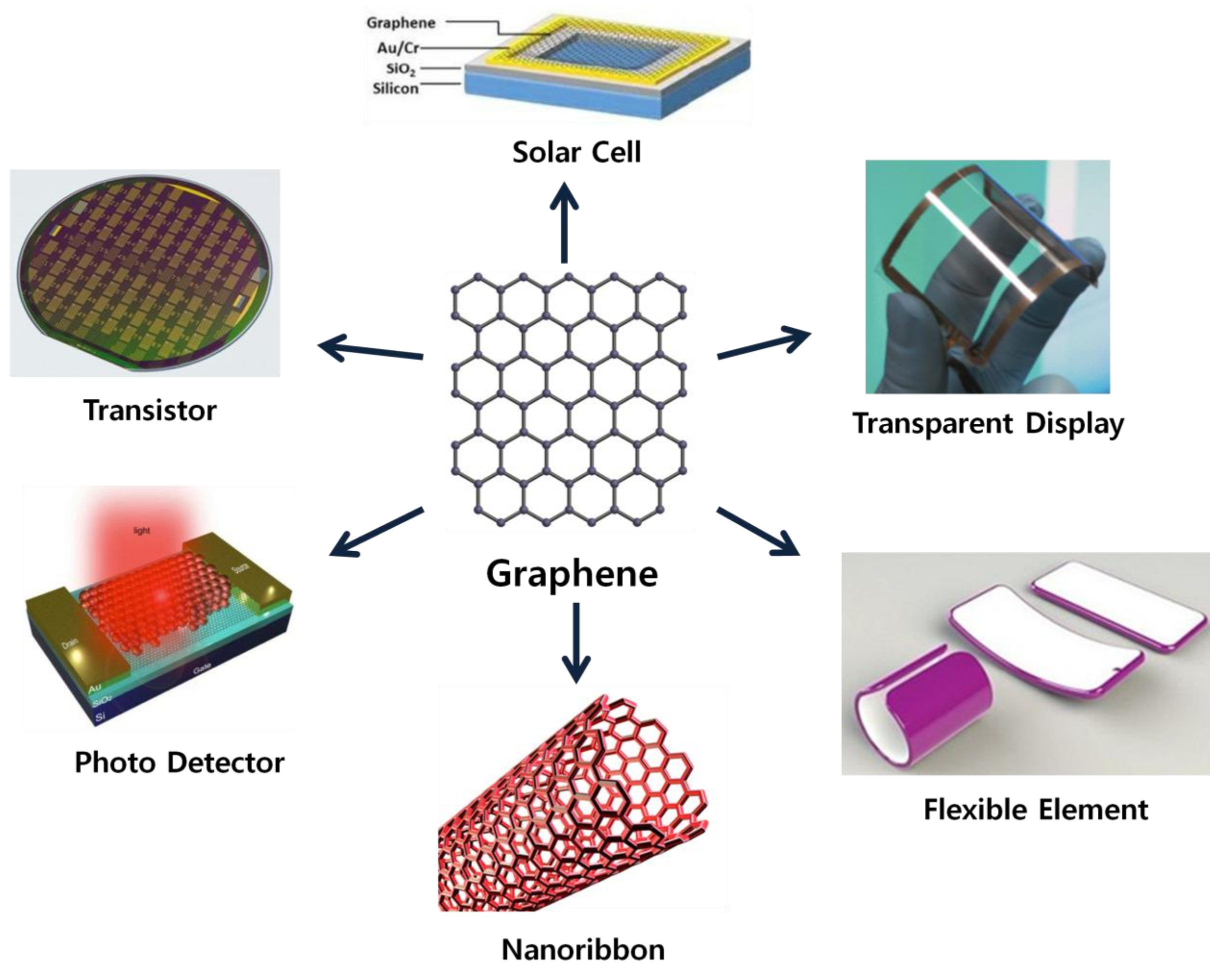

Figure 1-4: Applications of graphene

1.2.2. Properties of Graphene

The atomic structure of isolated, single-layer graphene was studied by transmission electron microscopy on sheets of graphene suspended between bars of a metallic grid [21]. Electron diffraction patterns showed the expected hexagonal lattice of graphene. Graphene processed using lithographic techniques is covered by photoresist residue, which must be cleaned to obtain atomic-resolution images [22]. Graphene sheets in solid form (density > 1 g/cm3) usually show evidence in diffraction for graphite's 0.34 nm layering. This is true even of some single-walled carbon nanostructures.[23] However, unlayered graphene with only rings has been found in the core of presolar graphite onions. Transmission electron microscope studies show faceting at defects in flat graphene sheets, and suggest a possible role in this unlayered - graphene for two-dimensional crystallization from a melt.

Graphene differs from most conventional three-dimensional materials. Intrinsic graphene is a semi-metal or zero-gap semiconductor. Understanding the electronic structure of graphene is the starting point for finding the band structure of graphite [24][25]. The E-k relation is linear for low energies near the six corners of the two-dimensional hexagonal Brillouin zone, leading to zero effective mass for electrons and holes. Due to this linear dispersion relation at low energies, electrons and holes near these six points, two of which are inequivalent, behave like relativistic particles described by the Dirac equation for spin 1/2 particles [26][27]. Hence, the electrons and holes are called Dirac fermions, and the six corners of the Brillouin zone are called the Dirac points. Experimental results from transport measurements show that graphene has a remarkably high electron mobility at room temperature, with reported values in excess of 15,000 $cm^2/V \cdot s$ [19]. Additionally, the symmetry of the experimentally measured conductance indicates that the mobilities for holes and electrons should be nearly the same. The mobility is nearly independent of temperature between 10 K and 100 K, [28][29] which implies that the dominant scattering mechanism is defect scattering. Scattering by the acoustic phonons of graphene places intrinsic limits on the room temperature mobility to 200,000 $cm^2/V \cdot s$ at a carrier density of 10^{12} cm^{-2} [30][31]. The corresponding resistivity of the graphene sheet would be 10^{-6} $\Omega \cdot cm$. This is less than the resistivity of silver, the lowest resistivity substance known at room temperature. However, for graphene on SiO^2 substrates, scattering of electrons by optical phonons of the substrate is a larger effect at room temperature than scattering by graphene’s own phonons. This limits the mobility to 40,000 $cm^2/V \cdot s$. Recent experiments have probed the influence of chemical dopants on the carrier mobility in graphene [32]. The doped graphene with various gaseous species (some acceptors, some donors), and found the initial undoped state of a graphene structure can be recovered by gently heating the graphene in vacuum. They reported that even for chemical dopant

concentrations in excess of 10^{12} cm^2 there is no observable change in the carrier mobility. It doped graphene with potassium in ultra high vacuum at low temperature. It was found that potassium ions act as expected for charged impurities in graphene, and can reduce the mobility 20 fold [33]. The mobility reduction is reversible on heating the graphene to remove the potassium. Due to its two-dimensional property, charge fractionalization is thought to occur in graphene. It may therefore be a suitable material for the construction of quantum computers using anyonic circuits [34].

Graphene's unique optical properties produce an unexpectedly high opacity for an atomic monolayer, with a startlingly simple value. It absorbs white light. This is a consequence of the unusual low-energy electronic structure of monolayer graphene that features electron and hole conical bands meeting each other at the Dirac point which is qualitatively different from more common quadratic massive bands [35]. Based on the Slonczewski-Weiss-McClure band model of graphite, the interatomic distance, hopping value and frequency cancel when the optical conductance is calculated using the Fresnel equations in the thin-film limit. This has been confirmed experimentally, but the measurement is not precise enough to improve on other techniques for determining the fine-structure constant. The band gap of graphene can be tuned from 0 to 0.25 eV (about 5 micrometre wavelength) by applying voltage to a dual-gate bilayer graphene field-effect transistor at room temperature [36]. The optical response of graphene nanoribbons has also been shown to be tunable into the terahertz regime by an applied magnetic field [37]. It has been shown that graphene / graphene oxide system exhibits electrochromic behavior, allowing tuning of both linear and ultrafast optical properties [38].

Bilayer graphene is two layers of graphene and it has been shown to have interesting electrical properties, such as the quantum hall effect, a tunable band gap, and potential for excitonic condensation [39] making them promising candidates for optoelectronic and nanoelectronic applications. Bilayer graphene typically can be found either in twisted configurations where two layer are rotated relative to each other or a graphitic Bernal stacked configurations where half the atoms in one layer lie atop half the atoms in the other. Stacking order and orientation greatly influence the optical and electronic properties of bilayer graphene. One way to synthesize bilayer graphene is via chemical vapor deposition, and can produce large area bilayer regions that almost exclusively conform to a Bernal stack geometry [40].

1.2.3. Process Methods

Graphene is an isolated atomic plane of graphite. Graphene planes become even better separated in intercalated graphite compounds. In 2004, physicists at the University of Manchester and the Institute for Microelectronics Technology, Chernogolovka, Russia, first isolated individual graphene planes by using adhesive tape [20]. They also measured electronic properties of the obtained flakes and showed their unique properties. In 2005 the same Manchester Geim group together with the Philip Kim group from Columbia University demonstrated that quasiparticles in graphene were massless Dirac fermions. These discoveries led to an explosion of interest in graphene. Since then, hundreds of researchers have entered the area, resulting in an extensive search for relevant earlier papers [Fig. 1-5].

- (a) Exfoliated graphene : In 2004, the Manchester group obtained graphene by micro-mechanical alleviation of graphite. They used adhesive tape to repeatedly split graphite crystals into increasingly thinner pieces. The tape with attached optically transparent flakes was dissolved in acetone, and, after a few further steps, the flakes including monolayers were sedimented on a silicon wafer. Individual atomic planes were then hunted in an optical microscope. A year later, the researchers simplified the technique and started using dry deposition, avoiding the stage when graphene floated in a liquid. Relatively large crystallites (first, only a few micrometres in size but, eventually, larger than 1 mm and visible by the naked eye) were obtained by the technique. It is often referred to as a scotch tape or drawing method. The latter name appeared because the dry deposition resembles drawing with a piece of graphite [21][41][42].

- (b) Epitaxial growth on SiC : Another method of obtaining graphene is to heat silicon carbide (SiC) to high temperatures (>1100 ℃) to reduce it to graphene [43][44]. This process produces epitaxial graphene with dimensions dependent upon the size of the SiC substrate (wafer). The face of the SiC used for graphene formation, silicon- or carbon-terminated, highly influences the thickness, mobility and carrier density of the graphene.Many important graphene properties have been identified in graphene produced by this method. Weak anti-localization is observed in this material and not in exfoliated graphene produced by the pencil-trace method. Extremely large, temperature-independent mobilities have been observed in SiC / epitaxial graphene. They approach those in exfoliated graphene placed on silicon oxide but still much lower than mobilities in suspended graphene produced by the drawing method. Epitaxial graphene on SiC can be patterned using standard microelectronics methods. The possibility of large integrated electronics on SiC / epitaxial graphene was first proposed in 2004, and a patent for graphene-based electronics was filed provisionally in 2003 and issued in 2006 [45]. Since then, important advances have been made. Band gap of

the epitaxial graphene can be tuned by irradiating with laser beams; modified graphene has a lot of advantages in device application.

- (c) Epitaxial growth on metal substrates : This method uses source and the atomic structure of a metal substrate to seed the growth of the graphene (epitaxial growth). Graphene grown on ruthenium doesn't typically yield a sample with a uniform thickness of graphene layers, and bonding between the bottom graphene layer and the substrate may affect the properties of the carbon layers. On the other hand, graphene grown on iridium is very weakly bonded, uniform in thickness, and can be made highly ordered. Like on many other substrates, graphene on iridium is slightly rippled. Due to the long-range order of these ripples, generation of mini-gaps in the electronic band-structure (Dirac cone) becomes visible [46]. High-quality sheets of few-layer graphene exceeding 1 cm^2 (0.2 sq) in area have been synthesized via chemical vapor deposition on thin nickel films with methane as a carbon source. These sheets have been successfully transferred to various substrates, demonstrating viability for numerous electronic applications [47][48].

(a) Exfoliated Graphene

(b) Epitaxial Growth on SiC

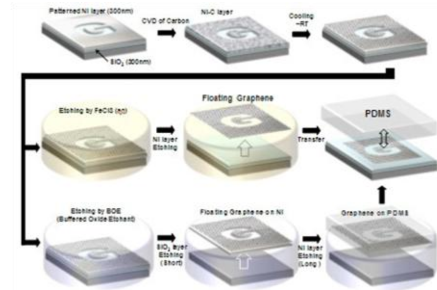

(c) Growth on Metal Substrates

Figure 1-5: Methods of graphene growth

1.3. Graphene on Silicon Carbide

SiC is one of the great potential semiconductor materials under harsh environments, because it has outstanding high temperature properties, chemical stability, and excellent radiation resistance [49]. Graphene, a single layer of carbon atoms from graphite, is a zero band gap semiconductor, has the ultimate two dimensional electron systems, possess many wonderful properties. To obtain graphene, it was used to mechanical exfoliation, chemical oxide reduction or exfoliation, and epitaxial graphene grown on SiC and metals [19]. However, the fabrication of quality graphene on a large scale is still difficult.

In this paper, we report an easy and controlled method by irradiating the electron beam (e-beam) on a SiC substrate. This research will propose a new method for graphene's formation. Graphene has been known for decades in many forms (mechanical exfoliation of graphite, epitaxially on SiC and metals) and a number of its properties were measured or inferred from related materials, like graphite and carbon nanotubes. But only recently was its potential as an electronic material recognized. Formation of graphene on silicon carbide has played a pivotal role in this development. In contrast to other candidate graphene fabrication methods, formation of graphene on SiC is produced in a simple, high-temperature annealing step on single-crystal SiC, which itself is an important electronic material. Subsequent graphene processing is straightforward and compatible with microelectronics procedures. In this letter, we introduce a relatively simple and well-controllable method to induce a large-scale epitaxial graphene with affordable electrical properties by directly irradiating e-beam on a SiC substrate in high vacuum environment (~10^{-5} Torr). In the common thermal annealing process to form graphene , the entire SiC substrate is heated to a high temperature around 1300-1600 ℃. Hence atoms sublimation could occur further deeper into the substrate from the surface. Differently from this process, we irradiated a continuous e-beam directly on SiC substrate. The merit of this process is low-temperature relatively. The temperature of SiC substrate surface was found to rise up to ~670 ℃ in the IR pyrometer reading during e-beam irradiation.

A new method is as follows [Fig. 1-6]. The process is formation of graphene lay by using electron beam irradiation. We obtain quality graphene layers and investigate formed graphene's properties on a SiC substrate. It is found that the electron beam irradiation can appear the sublimation of Si from the surface of a SiC substrate. The changes on the surface of a SiC substrate are observed after e-beam irradiation. In the e-beam irradiation process, the e-beam energy is injected towards the surface of a SiC substrate and being dispersed on the surface of a SiC substrate. After all, there is a sublimation of Si atoms occurs and only remain C atoms on the surface of a SiC substrate.

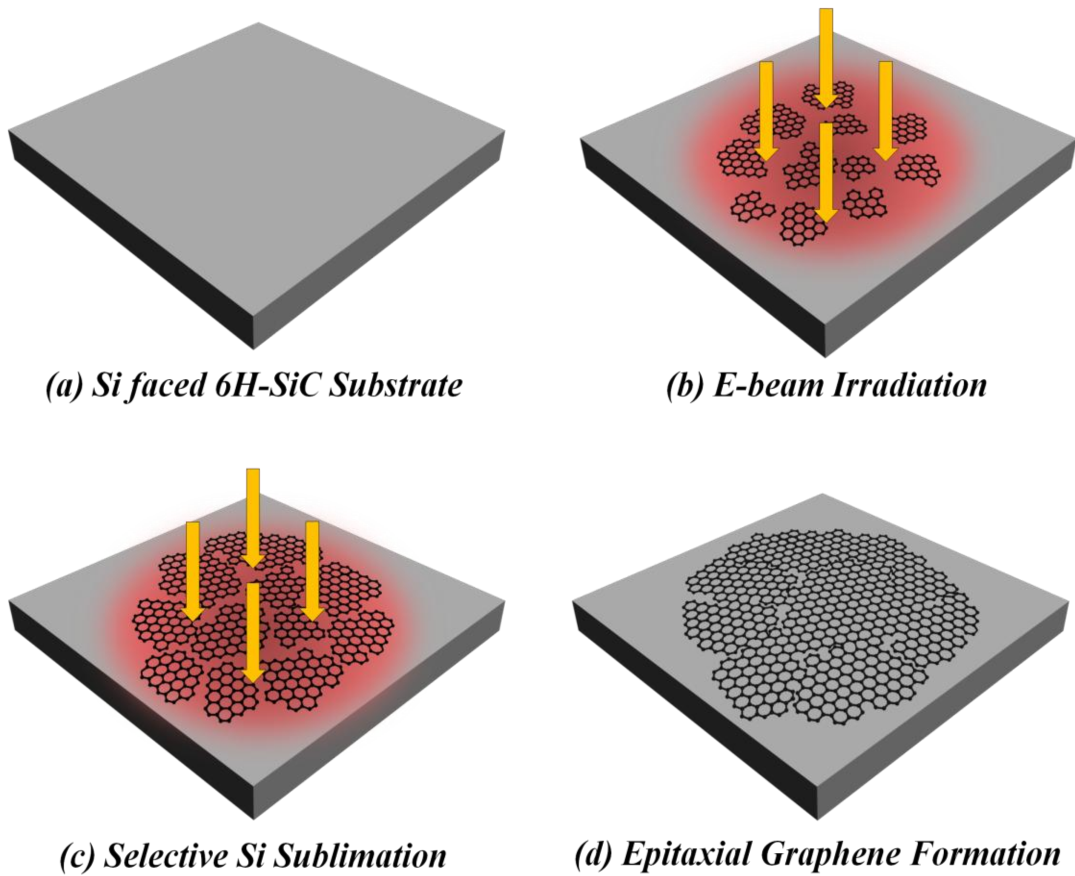

Figure 1-6: Schematic diagrams showing the formation of epitaxial graphene on 6H-SiC substrate by irradiating e-beam. (a) 6H-SiC substrate before e-beam irradiation. (b) The ealy stage of e-beam irradiation with many small graphene islands distributed randomly on the sample surface. (c) The lateral growth of the formed graphene islands as e-beam irradiation time increases. (d) The 6H-SiC substrate after e-beam irradiation is completed where epitaxial graphene layers cover most of the e-beam irradiated area.

Chapter II

Approaches & Measurement

This chapter demonstrates that formation of graphene layer on the surface of a 6H-SiC substrate by using electron beam (e-beam) irradiation. The e-beam is irradiated by using a commercial electron beam evaporator with acceleration voltage 8kV in high vacuum environment. Raman spectrum measurements show all relevant peaks (D, G, 2D) clearly, confirming the formation of epitaxial graphene layers. The elemental composition of the epitaxial graphene layer is measured with Auger Electron Spectroscopy and X-ray Photoelectron Spectroscopy. The sheet resistance of the epitaxial graphene layer which is measured by forming CTLM (Circular Transmission Line Model) patterns on the irradiated 6H-SiC surface is found to decrease at least 1000 times, compared with the original 6H-SiC substrate. Also, the quality of the epitaxial graphene layer in terms of Raman spectrum and sheet resistance is found to be improved noticeably as the electron fluence (e/cm^2) is increased by making the irradiation time longer.

2.1. Experimental Method

This approach has to use electron beam for irradiation on the SiC substrate. And it is required environment of low acceleration voltage in a vacuum. So, it is selected electron beam evaporator (e-beam evaporator). The e-beam evaporator process falls into a larger category of Micro-Electro-Mechanical Systems (MEMS) processes known as Physical Vapor Deposition (PVD). Deposition processes are used to release a material from a source and transfer that material to a substrate, forming a thin film or coating. PVD processes are commonly used for the deposition of metals, because they can be performed at lower process risk and cheaper in regards to materials cost that Chemical Vapor Deposition (CVD). In the evaporation process, a block of the material (source) to be deposited is heated to the point where it starts to boil and evaporate. Then it is allowed to condense on the substrate—the material that you want to coat. This process takes place inside a vacuum chamber, enabling the molecules to evaporate freely in the chamber, where they then condense on all surfaces. For e-beam evaporation, an electron beam is used to heat the source material and cause evaporation. e-beam evaporator is a commonly used process for coating lenses and filters with anti-reflection, scratch-resistant or other specialized coatings. The process is also commonly used for coating insulating and resistor films on electronic components. Multi-layer coatings can be deposited in one duty cycle. The e-beam evaporator process typically involves the following components:

- Electron beam evaporation gun
- A system controller
- Power supply
- Crucibles for the evaporation material
- Materials for evaporation
- Material to be coated
- The entire process takes place inside of a vacuum chamber.

This experiment is used electron beam evaporation gun, power supply and crucible. The SiC sample is inserted in the crucible and irradiated by using electron beam gun in the vacuum [Fig. 2-1]. We propose the e-beam irradiation method on the surface of a SiC by using the e-beam evaporator. The e-beam in the evaporator is originally used for melting metal sources. We try to use e-beam equipment as not melting but irradiation purposes.

The research is used 6H-SiC substrate. Single crystalline On-axis, Si terminated n-type 6H-SiC wafers are obtained from Cree, Inc. The samples are rinsed with HF and deionized water (1:10) to remove the surface native oxide before being put into the vacuum chamber. The e-beam irradiation was performed in high vacuum environment (~10^{-6} Torr) at an acceleration voltage of 8kV. The e-beam irradiated area was ~ 5 mm Χ 5 mm and the current was fixed to be ~2mA. The only experimental variable was the irradiation time that determined electron fluency (number of electrons per unit area). The four different irradiation times (corresponding electron fluencies) are 0.5 hr (9×10^{19} e/cm^2), 1.0 hr (1.8×10^{20} e/cm^2), 1.5 hr (2.7×10^{20} e/cm^2), and 2.0 hr (3.6×10^{20} e/cm^2). The parameter of study is as follows [Table 2-1]. The sample temperature was not adjusted intentionally and left at room temperature in the beginning. However, the temperature of sample surface was found to rise up to ~670 ℃ in the IR pyrometer reading during e-beam irradiation [Fig. 2-2]. After the e-beam irradiation was completed, the sample was cooled down to room temperature in vacuum.

	Sample 1	Sample 2	Sample 3	Sample 4
Accelerate Voltage (kV)	8	8	8	8
Current (mA)	2	2	2	2
Irradiation Time (hr)	0.5	1	1.5	2
Fluencies (e/cm^2)	9×10^{19}	1.8×10^{20}	2.7×10^{20}	3.6×10^{20}

Table 2-1: Parameter of e-beam irradiation

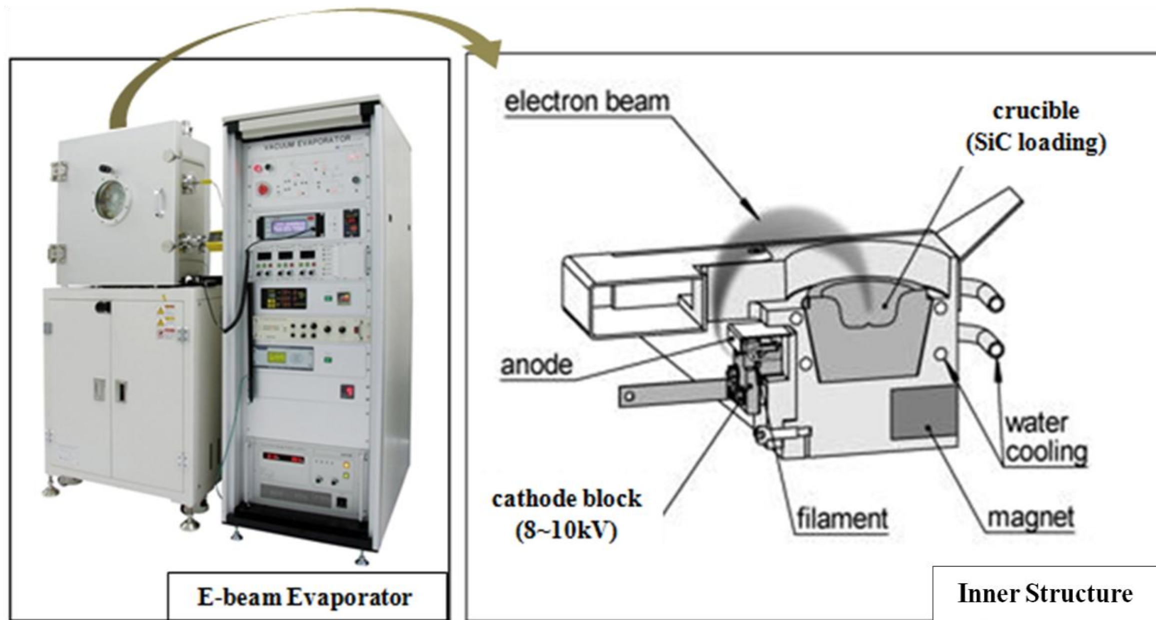

Figure 2-1: Appearance and inner structure of e-beam evaporator

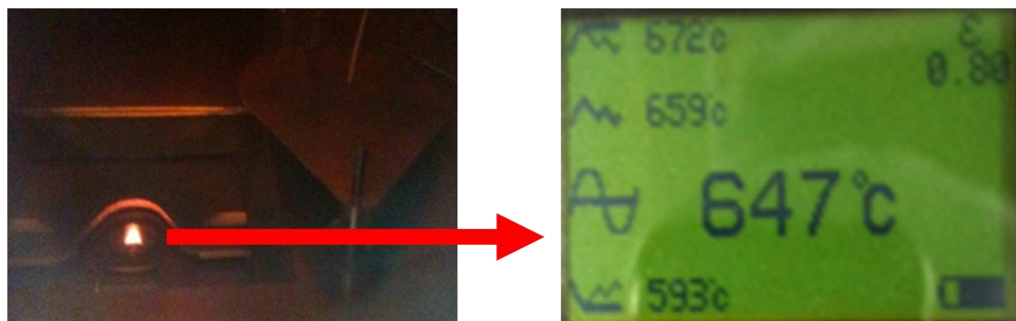

Figure 2-2: Image and temperature of e-beam irradiation

2.2. Research Results

This research focuses on the aspects of textural and electrical characteristics of formed graphene on 6H-SiC by using e-beam irradiation. It is proved whether irradiated layer is the graphene layer by using Raman Spectrum, Auger Electron Spectroscopy, X-ray Photoelectron Spectroscopy and Transmission Electron Microscopy. And it is made Circular Transmission Line Measurement (CTLM) structure on irradiated 6H-SiC substrate, is be can measure sheet resistance and contact resistance of graphene layer.

2.2.1. Structural and Compositional Analysis

The first category includes spectrum analysis of graphene layer formed on 6H-SiC substrate by using e-beam irradiation. The measurement equipments are Raman Spectrum, Auger Electron Spectroscopy, X-ray Photoelectron Spectroscopy

The second category is shown thickness of formed graphene layer by measuring Transmission Electron Microscopy.

2.2.1.1. Raman Spectrum Analysis

First, to identify graphene layers, it uses Raman spectroscopy. Raman spectroscopy is a spectroscopic technique used to study vibrational, rotational, and other low-frequency modes in a system [50]. It relies on inelastic scattering, or Raman scattering, of monochromatic light, usually from a laser in the visible, near infrared, or near ultraviolet range. The laser light interacts with molecular vibrations, phonons or other excitations in the system, resulting in the energy of the laser photons being shifted up or down. The shift in energy gives information about the vibrational modes in the system. Infrared spectroscopy yields similar, but complementary, information.

Typically, a sample is illuminated with a laser beam. Light from the illuminated spot is collected with a lens and sent through a monochromator. Wavelengths close to the laser line due to elastic Rayleigh scattering are filtered out while the rest of the collected light is dispersed onto a detector. Spontaneous Raman scattering is typically very weak, and as a result the main difficulty of Raman spectroscopy is separating the weak inelastically scattered light from the intense Rayleigh scattered laser light [51][52]. Historically, Raman spectrometers used holographic gratings and multiple dispersion stages to achieve a high degree of laser rejection. In the past, photomultipliers were the detectors of choice for dispersive Raman setups, which resulted in long acquisition times. However, modern instrumentation almost universally employs notch or edge filters for laser rejection and spectrographs either axial transmissive (AT), Czerny-Turner (CT) monochromator, or FT (Fourier

transform spectroscopy based), and CCD detectors. There are a number of advanced types of Raman spectroscopy, including surface-enhanced Raman, resonance Raman, tip-enhanced Raman, polarised Raman, stimulated Raman (analogous to stimulated emission), transmission Raman, spatially offset Raman, and hyper Raman. The Raman effect occurs when light impinges upon a molecule and interacts with the electron cloud and the bonds of that molecule. For the spontaneous Raman effect, which is a form of light scattering, a photon excites the molecule from the ground state to a virtual energy state. When the molecule relaxes it emits a photon and it returns to a different rotational or vibrational state. The difference in energy between the original state and this new state leads to a shift in the emitted photon's frequency away from the excitation wavelength. The Raman effect, which is a light scattering phenomenon, should not be confused with absorption (as with fluorescence) where the molecule is excited to a discrete (not virtual) energy level. If the final vibrational state of the molecule is more energetic than the initial state, then the emitted photon will be shifted to a lower frequency in order for the total energy of the system to remain balanced. This shift in frequency is designated as a Stokes shift. If the final vibrational state is less energetic than the initial state, then the emitted photon will be shifted to a higher frequency, and this is designated as an Anti-Stokes shift. Raman scattering is an example of inelastic scattering because of the energy transfer between the photons and the molecules during their interaction. A change in the molecular polarization potential or amount of deformation of the electron cloud with respect to the vibrational coordinate is required for a molecule to exhibit a Raman effect. The amount of the polarizability change will determine the Raman scattering intensity. The pattern of shifted frequencies is determined by the rotational and vibrational states of the sample. This dependence on the polarizability differs from Infrared spectroscopy where the interaction between the molecule and light is determined by the dipole moment; this contrasting feature allows to analyze transitions that might not be IR active via Raman spectroscopy, as exemplified by the rule of mutual exclusion in centrosymmetric molecules.

It presents the changes of Raman spectra for before and after irradiation [Fig. 2-3a]. The strong Raman peaks around 1510 cm^{-1} and 1710 cm^{-1} are shown in the bare 6H-SiC. Firstly, in such cases the bare 6H-SiC substrate is irradiated by e-beam during 0.5 hr, the Raman peaks present around 1350 cm^{-1} and 1580 cm^{-1}. The 1350 cm^{-1} and 1580 cm^{-1} peaks indicate D and G peak respectively. And the bare 6H-SiC's Raman peaks(1510 cm^{-1} and 1710 cm^{-1}) are decreased relatively. In case it increased the irradiation time up to 1 hr, the Raman peak is shown around 2700cm^{-1} slightly. The 2700cm^{-1} peak indicates 2D peak. Also the D and G peaks are increased a little more. In the case of the irradiation time of 1.5 hr, the 2D peak is shown distinctly. Lastly, in case the irradiation time is increased up to 2 hr, the G, 2D peaks are shown some more sharply and obviously. And it is found that the D peak decreases considerably and the bare 6H-SiC's Raman peaks disappear. To show obviously the Raman peaks, we subtract the bare 6H-SiC's Raman data from each 0.5 hr, 1 hr, 1.5 hr, and 2 hr Raman data.

The D and G peaks are observed in the 0.5 hr Raman data and we can show definitely the D, G, and 2D peaks in the 1 hr, 1.5 hr, and 2 hr Raman data. During 2 hr irradiation time, D peak is decreased and 2D peak is increased greatly [Fig. 2-3b]. It is assumed that the irradiated 6H-SiC surface presents the Raman spectra of graphene. The more irradiation time is increased, the more quality graphene layers are formed equally and perfectly. An existence of D peak in the Raman spectra of graphene layers, which is just because of the irradiation defects by e-beam.

Another important information that we can obtain from the measured Raman spectrum is that the 2D peak is quite symmetric and can be fitted to a single Lorentzian with a FWHM (Full Width Half Maximum) larger than a monolayer graphene. This indicates that the epitaxial graphene induced by e-beam irradiation is turbostratic, meaning that the stacking of graphene layers is rotationally random with respect to one another along the stacking direction. The mechanism that the epitaxial graphene induced by e-beam irradiation becomes turbostratic is not clear at this moment. Hence more detailed studies to investigate the physical environments near the surface of SiC substrate obtained by e-beam irradiation and their influence on the formation of epitaxial graphene are necessary [Fig. 2-4].

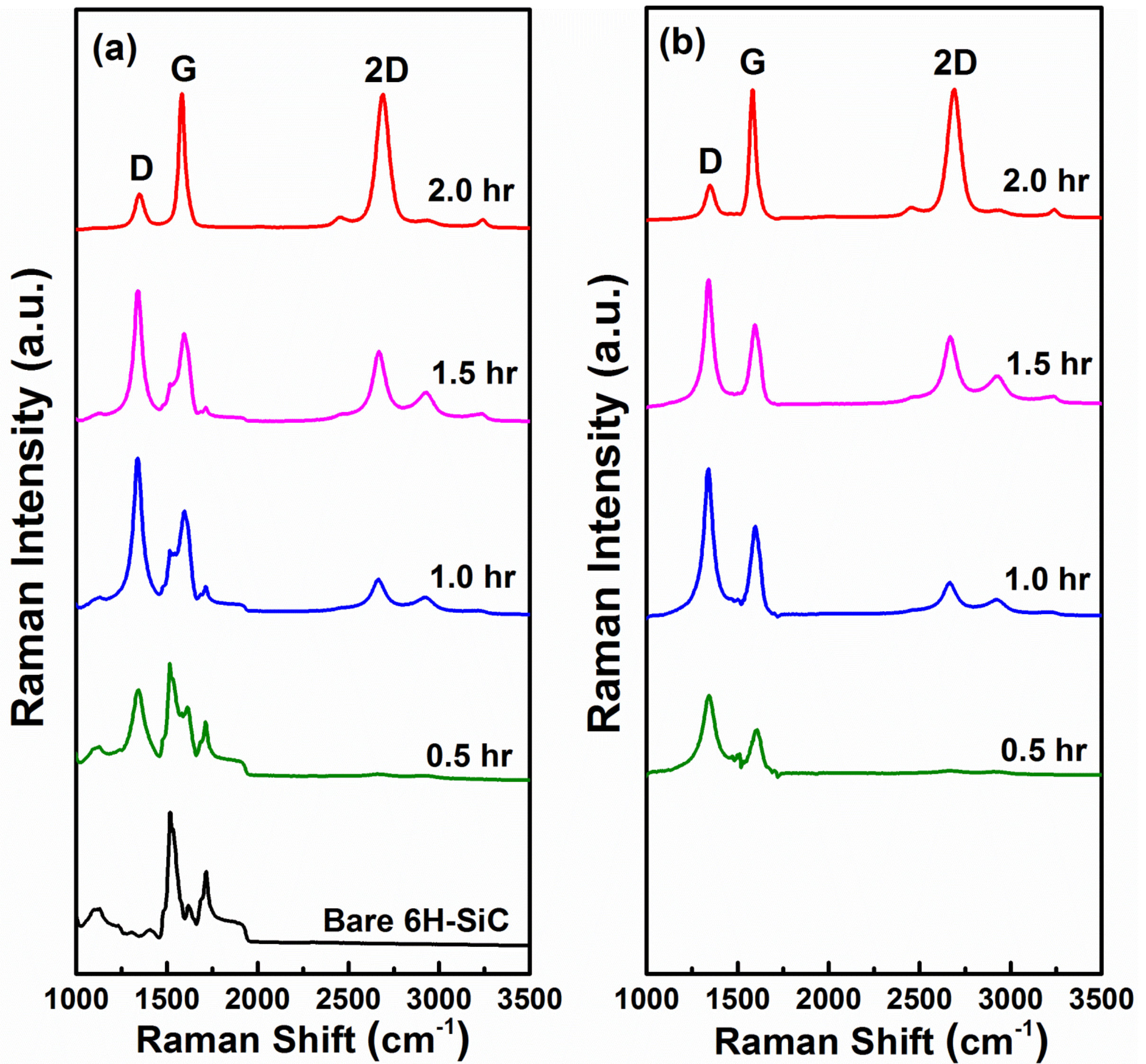

Figure 2-3: Raman shifts of graphene layers. (a) The original Raman spectra measured on a 6H-SiC substrate as a function of e-beam irradiation time. (b) The corresponding Raman spectra with the Raman signals coming from the 6H-SiC substrate subtracted.

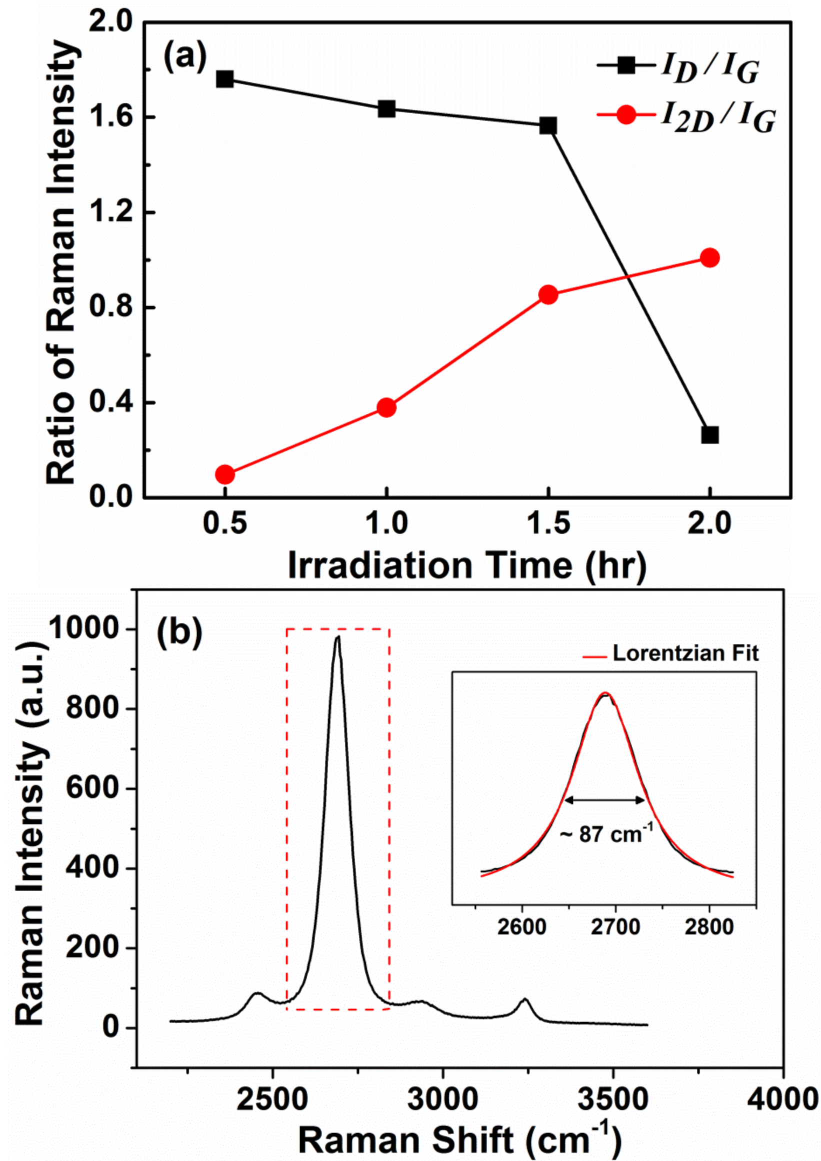

Figure 2-4: (a) I_D/I_G & I_{2D}/I_G ration. The relative Raman intensities of the D and 2D peaks compared to the G peak as e-beam irradiation time increases (b) 2D peak Lorentzian fitted data of graphene layers. The zoom-in of the 2D peak measured on the 6H-SiC substrate irradiated by e-beam for 2 hours with its single Lorentzian fit.

2.2.1.2. Transmission Electron Microscopy Analysis

To measure thickness of graphene layers, use the Transmission Electron Microscopy (TEM). TEM is a microscopy technique whereby a beam of electrons is transmitted through an ultra thin specimen, interacting with the specimen as it passes through. An image is formed from the interaction of the electrons transmitted through the specimen; the image is magnified and focused onto an imaging device, such as a fluorescent screen, on a layer of photographic film, or to be detected by a sensor such as a CCD camera. TEMs are capable of imaging at a significantly higher resolution than light microscopes, owing to the small de Broglie wavelength of electrons. This enables the instrument's user to examine fine detail even as small as a single column of atoms, which is tens of thousands times smaller than the smallest resolvable object in a light microscope. TEM forms a major analysis method in a range of scientific fields, in both physical and biological sciences. TEMs find application in cancer research, virology, materials science as well as pollution, nanotechnology, and semiconductor research. At smaller magnifications TEM image contrast is due to absorption of electrons in the material, due to the thickness and composition of the material. At higher magnifications complex wave interactions modulate the intensity of the image, requiring expert analysis of observed images. Alternate modes of use allow for the TEM to observe modulations in chemical identity, crystal orientation, electronic structure and sample induced electron phase shift as well as the regular absorption based imaging. TEM is composed of several components, which include a vacuum system in which the electrons travel, an electron emission source for generation of the electron stream, a series of electromagnetic lenses, as well as electrostatic plates. The latter two allow the operator to guide and manipulate the beam as required. Also required is a device to allow the insertion into, motion within, and removal of specimens from the beam path. Imaging devices are subsequently used to create an image from the electrons that exit the system. To increase the mean free path of the electron gas interaction, a standard TEM is evacuated to low pressures, typically on the order of 10^{-4} Pa [53]. The need for this is twofold. The allowance for the voltage difference between the cathode and the ground without generating an arc, and secondly to reduce the collision frequency of electrons with gas atoms to negligible levels—this effect is characterised by the mean free path. TEM components such as specimen holders and film cartridges must be routinely inserted or replaced requiring a system with the ability to re-evacuate on a regular basis. As such, TEMs are equipped with multiple pumping systems and airlocks and are not permanently vacuum sealed. The vacuum system for evacuating a TEM to an operating pressure level consists of several stages. Initially a low or roughing vacuum is achieved with either a rotary vane pump or diaphragm pumps bringing the TEM to a sufficiently low pressure to allow the operation of a turbomolecular or diffusion pump which brings the TEM to its high vacuum level necessary for operations. To allow for the low vacuum pump to not require continuous operation, while continually operating the

turbomolecular pumps, the vacuum side of a low-pressure pump may be connected to chambers which accommodate the exhaust gases from the turbomolecular pump [54]. Sections of the TEM may be isolated by the use of gate valves, to allow for different vacuum levels in specific areas, such as a higher vacuum of 10^{-4} to 10^{-7} Pa or higher in the electron gun in high-resolution or field-emission TEMs.

TEM specimen stage designs include airlocks to allow for insertion of the specimen holder into the vacuum with minimal increase in pressure in other areas of the microscope. The specimen holders are adapted to hold a standard size of grid upon which the sample is placed or a standard size of self-supporting specimen. Standard TEM grid sizes are a 3.05 mm diameter ring, with a thickness and mesh size ranging from a few to 100 μm. The sample is placed onto the inner meshed area having diameter of approximately 2.5 mm. Usual grid materials are copper, molybdenum, gold or platinum. This grid is placed into the sample holder, which is paired with the specimen stage. A wide variety of designs of stages and holders exist, depending upon the type of experiment being performed. In addition to 3.05 mm grids, 2.3 mm grids are sometimes, if rarely, used. These grids were particularly used in the mineral sciences where a large degree of tilt can be required and where specimen material may be extremely rare. Electron transparent specimens have a thickness around 100 nm, but this value depends on the accelerating voltage. Once inserted into a TEM, the sample often has to be manipulated to present the region of interest to the beam, such as in single grain diffraction, in a specific orientation. To accommodate this, the TEM stage includes mechanisms for the translation of the sample in the XY plane of the sample, for Z height adjustment of the sample holder, and usually for at least one rotation degree of freedom for the sample. Thus a TEM stage may provide four degrees of freedom for the motion of the specimen. Most modern TEMs provide the ability for two orthogonal rotation angles of movement with specialized holder designs called double-tilt sample holders. Of note however is that some stage designs, such as top-entry or vertical insertion stages once common for high resolution TEM studies, may simply only have X-Y translation available. The design criteria of TEM stages are complex, owing to the simultaneous requirements of mechanical and electron-optical constraints and have thus generated many unique implementations. A TEM stage is required to have the ability to hold a specimen and be manipulated to bring the region of interest into the path of the electron beam. As the TEM can operate over a wide range of magnifications, the stage must simultaneously be highly resistant to mechanical drift, with drift requirements as low as a few nm/minute while being able to move several μm/minute, with repositioning accuracy on the order of nanometers [55]. Earlier designs of TEM accomplished this with a complex set of mechanical down gearing devices, allowing the operator to finely control the motion of the stage by several rotating rods. Modern devices may use electrical stage designs, using screw gearing in concert with

stepper motors, providing the operator with a computer-based stage input, such as a joystick or trackball.

HR-TEM image (cross-sectional) were taken to directly observe the formed epitaxial graphene layers. The result of formed graphene layers thickness measurement is verified 7 ~ 8 layers of graphene [Fig 2-5(a)]. It is checked out that thickness of 1 layer is approximately 0.32 nm [Fig 2-5(b)]. TEM images (cross-sectional) were taken to directly observe the formed epitaxial graphene layers. Shows the HR-TEM image measured on the 6H-SiC sample irradiated by e-beam for 2 hours where 7~8 layers brighter than others are found clearly on the sample surface as indicated in the figure. According to the profile of TEM signal intensity, the spacing between two adjacent brighter layers is ~0.32 nm. This measured spacing is very close to the known spacing of graphene layers, indicating the actual formation of epitaxial graphene. In order to confirm that those brighter layers are really graphene layers, AES (Auger Electron Spectroscopy) and XPS (X-ray Photoemission Spectroscopy) measurements were performed to analyze atomic composition of the e-beam irradiated area.

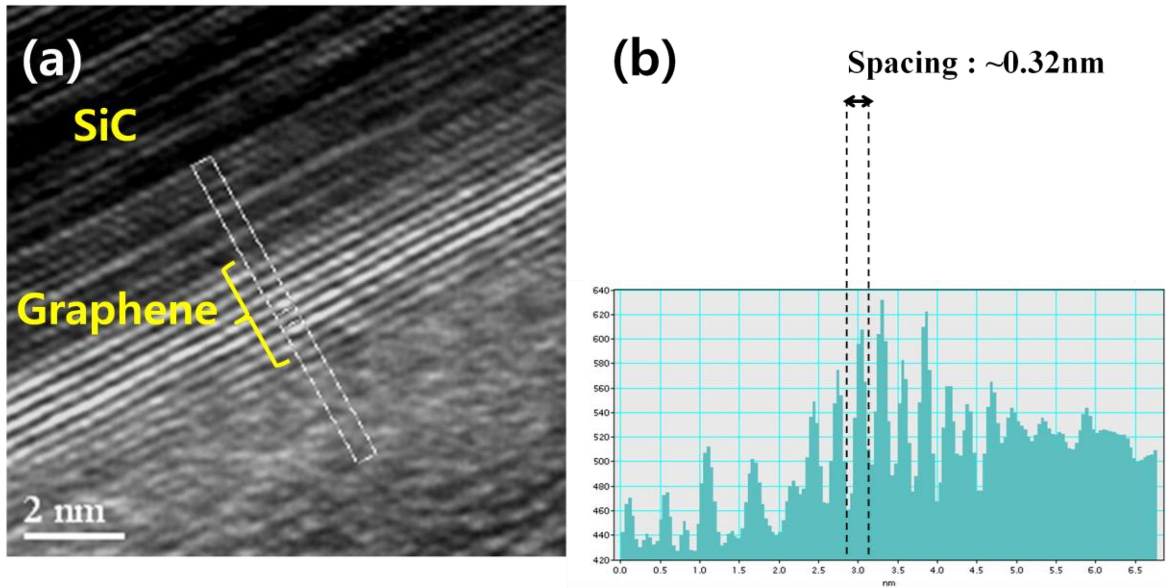

Figure 2-5: Measurement of graphene's thickness by using TEM. (a) Cross-sectional HR-TEM image of the 6H-SiC substrate irradiated by e-beam for 2 hours where 7~8 layers brighter than the others can be seen on the surface as indicated in the figure. (b) The spacing between adjacent brighter layers, measured to be ~ 0.32 nm in the profile of HR-TEM signal intensity, confirms that the brighter layers are actually graphene layers.

2.2.1.3. Auger Electron Spectroscopy Analysis

To reveal the element of the formed graphene layers on SiC surface by the e-beam irradiation, we use Auger Electron Spectroscopy (AES). AES is a common analytical technique used specifically in the study of surfaces and, more generally, in the area of materials science. Underlying the spectroscopic technique is the Auger effect, as it has come to be called, which is based on the analysis of energetic electrons emitted from an excited atom after a series of internal relaxation events. AES has become a practical and straightforward characterization technique for probing chemical and compositional surface environments and has found applications in metallurgy, gas-phase chemistry, and throughout the microelectronics industry [56]. The Auger effect is an electronic process at the heart of AES resulting from the inter- and intrastate transitions of electrons in an excited atom. When an atom is probed by an external mechanism, such as a photon or a beam of electrons with energies in the range of 2 keV to 50 keV, a core state electron can be removed leaving behind a hole. As this is an unstable state, the core hole can be filled by an outer shell electron, whereby the electron moving to the lower energy level loses an amount of energy equal to the difference in orbital energies. The transition energy can be coupled to a second outer shell electron which will be emitted from the atom if the transferred energy is greater than the orbital binding energy [57]. There are a number of electron microscopes that have been specifically designed for use in Auger spectroscopy, these are termed Scanning Auger microscopes (SAM) and can produce high resolution, spatially resolved chemical images. SAM images are obtained by stepping a focused electron beam across a sample surface and measuring the intensity of the Auger peak above the background of scattered electrons. The intensity map is correlated to a gray scale on a monitor with whiter areas corresponding to higher element concentration. In addition, sputtering is sometimes used with Auger spectroscopy to perform depth profiling experiments. Sputtering removes thin outer layers of a surface so that AES can be used to determine the underlying composition. Depth profiles are shown as either Auger peak height vs. sputter time or atomic concentration vs. depth. Precise depth milling through sputtering has made profiling an invaluable technique for chemical analysis of nanostructured materials and thin films. AES is also used extensively as an evaluation tool on and off fab lines in the microelectronics industry, while the versatility and sensitivity of the Auger process makes it a standard analytical tool in research labs. Despite the advantages of high spatial resolution and precise chemical sensitivity attributed to AES, there are several factors that can limit the applicability of this technique, especially when evaluating solid specimens. One of the most common limitations encountered with Auger spectroscopy are charging effects in non-conducting samples. Charging results when the number of secondary electrons leaving the sample is different to the number of incident electrons, giving rise to a net polarity at the surface. Both positive and negative surface charges severely alter the yield of electrons emitted from the sample and hence distort the measured Auger peaks. To complicate matters,

neutralization methods employed in other surface analysis techniques, such as secondary ion mass spectrometry (SIMS), are not applicable to AES, as these methods usually involve surface bombardment with either electrons or ions. Several processes have been developed to combat the issue of charging, though none of them is ideal and still make quantification of AES data difficult. One such technique involves depositing conductive pads near the analysis area to minimize regional charging. However, this type of approach limits SAM applications as well as the amount of sample material available for probing. A related technique involves thinning or "dimpling" a non-conductive layer with Ar+ ions and then mounting the sample to a conductive backing prior to AES. This method has been debated, with claims that the thinning process leaves elemental artifacts on a surface and/or creates damaged layers that distort bonding and promote chemical mixing in the sample. As a result, the compositional AES data is considered suspect. The most common setup to minimize charging effects includes use of a glancing angle (~10°) electron beam and a carefully tuned bombarding energy (between 1.5 keV and 3 keV). Control of both the angle and energy can subtly alter the number of emitted electrons vis-à-vis the incident electrons and thereby reduce or altogether eliminate sample charging. In addition to charging effects, AES data can be obscured by the presence of characteristic energy losses in a sample and higher order atomic ionization events. Electrons ejected from a solid will generally undergo multiple scattering events and lose energy in the form of collective electron density oscillations called plasmons. If plasmon losses have energies near that of an Auger peak, the less intense Auger process may become dwarfed by the plasmon peak. As Auger spectra are normally weak and spread over many eV of energy, they are difficult to extract from the background and in the presence of plasmon losses, deconvolution of the two peaks becomes extremely difficult. For such spectra, additional analysis through chemical sensitive surface techniques like x-ray photoelectron spectroscopy (XPS) is often required to disentangle the peaks. Sometimes an Auger spectrum can also exhibit "satellite" peaks at well-defined off-set energies from the parent peak. Origin of the satellites is usually attributed to multiple ionization events in an atom or ionization cascades in which a series of electrons is emitted as relaxation occurs for core holes of multiple levels. The presence of satellites can distort the true Auger peak and/or small peak shift information due to chemical bonding at the surface. Several studies have been undertaken to further quantify satellite peaks. Despite these sometimes substantial drawbacks, Auger electron spectroscopy is a widely used surface analysis technique that has been successfully applied to many diverse fields ranging from gas phase chemistry to nanostructure characterization. Very new class of high-resolving electrostatic energy analyzers recently developed the face-field analyzers (FFA) can be used for remote electron spectroscopy of distant surfaces or surfaces with large roughness or even with deep dimples. These instruments are designed as if to be specifically used in combined scanning electron microscopes (SEMs). "FFA" in principle have no perceptible end-fields, which usually distort focusing in most of analysers known, for example, well known CMA [58][59].

Sensitivity, quantitative detail, and ease of use have brought AES from an obscure nuisance effect to a functional and practical characterization technique in just over fifty years. With applications both in the research laboratory and industrial settings, AES will continue to be a cornerstone of surface-sensitive electron-based spectroscopies. It shows the C KLL, O KLL, and Si KLL AES spectra of the bare 6H-SiC and the irradiated 6H-SiC during 2 hr [Fig 2-6 ~ 2-9]. It is clear that the intensity of the O KLL and Si KLL auger electron is attenuated with the irradiation by e-beam, whereas that in the C KLL electron increased. The C KLL (263 eV), O KLL (503 eV), and Si KLL (1557, 1577, 1597, 1614 eV) peaks are found in the bare Si terminated 6H-SiC. After e-beam irradiation, O KLL and Si KLL peaks disappear and C KLL peak is increased up to about 1.5 times. As shown in the figures, Si atoms disappear almost completely after e-beam irradiation and only C atoms are left near the sample surface. So we verify that the carbon layers are formed on the SiC surface by e-beam irradiation. The sublimation of Si on the 6H-SiC surface occurs and quality carbon layers i.e. graphene layers are formed by using e-beam irradiation. This measured AES spectra strongly indicates that any layers induced on the sample surface by e-beam irradiation should be composed of C atoms and hence the brighter layers observed in the TEM image are really graphene layers.

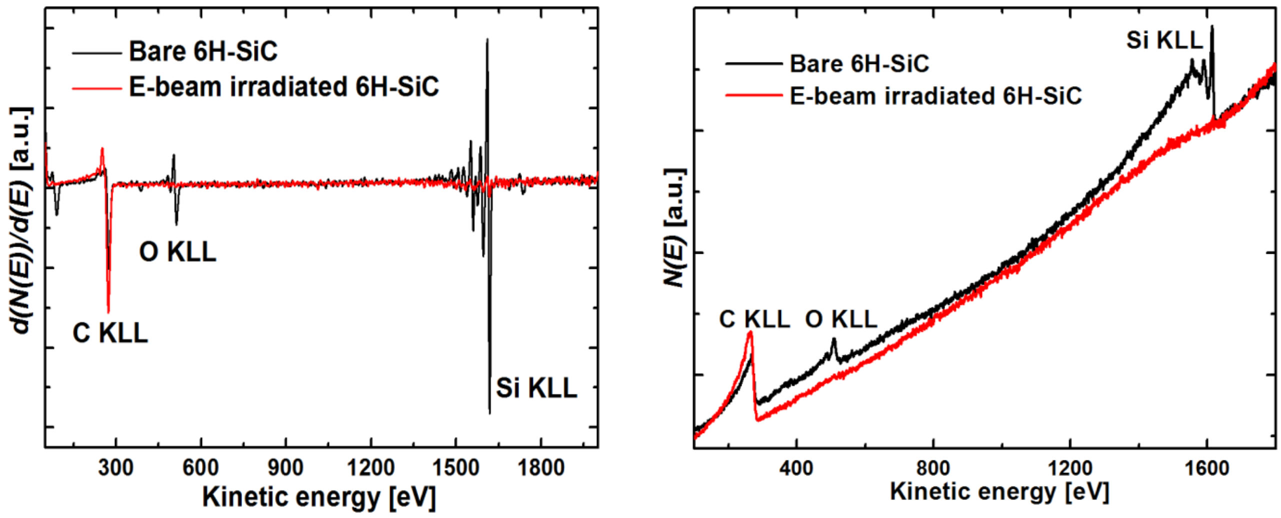

Figure 2-6: AES spectra of 6H-SiC and graphene layer (Differentiated & Undifferentiated Mode). After e-beam irradiation (2 hr), O KLL (503 eV) and Si KLL (1557, 1577, 1597, 1614 eV) peaks disappear and C KLL (263 eV) peak is increased up to about 1.5 times.

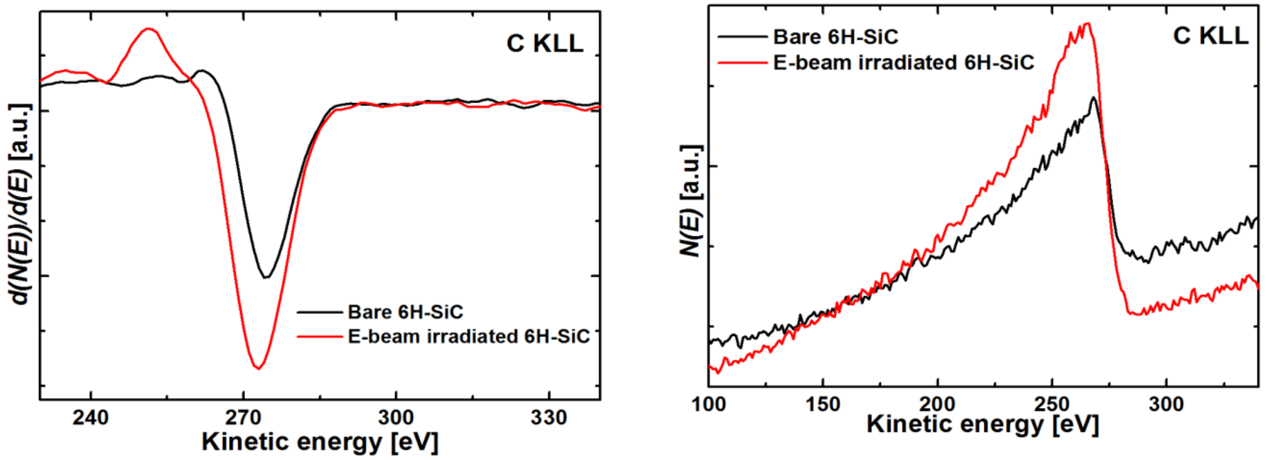

Figure 2-7: AES spectra - C range (Differentiated & Undifferentiated Mode)

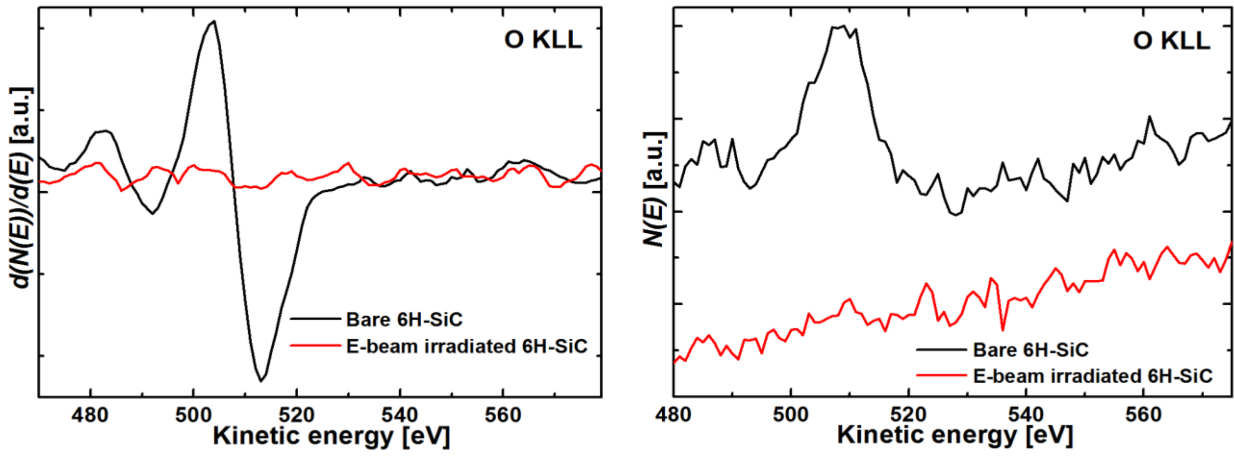

Figure 2-8: AES spectra - O range (Differentiated & Undifferentiated Mode)

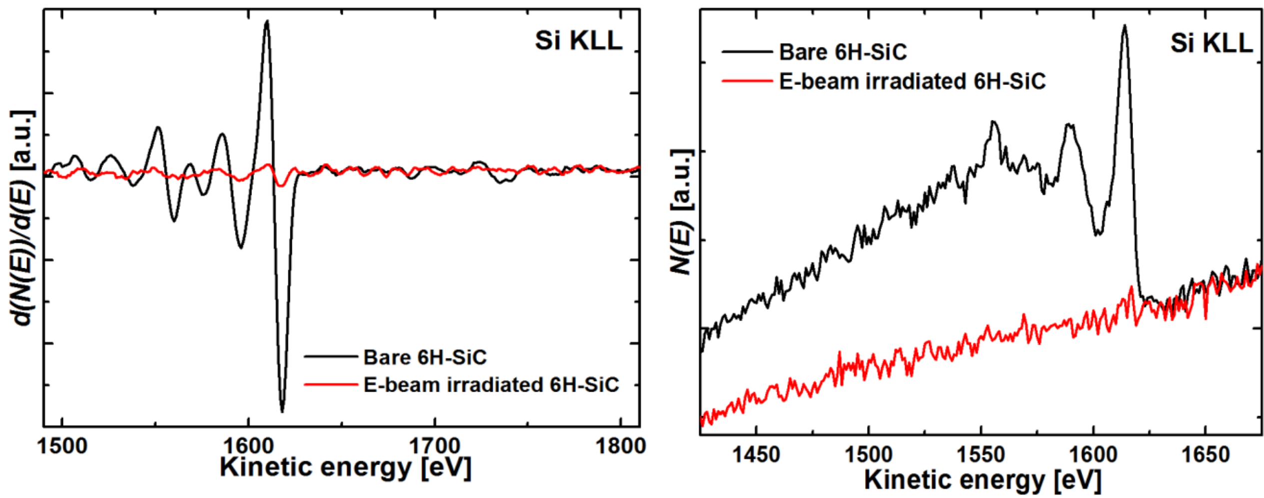

Figure 2-9: AES spectra - Si range (Differentiated & Undifferentiated Mode)

2.2.1.4. X-ray Photoelectron Spectroscopy Analysis

We measure X-ray Photoelectron Spectroscopy (XPS) to prove definitely the existence of graphene layers. The XPS is one of the important techniques for studying surface elements and bonding energy of materials. XPS is a quantitative spectroscopic technique that measures the elemental composition, empirical formula, chemical state and electronic state of the elements that exist within a material [60]. XPS spectra are obtained by irradiating a material with a beam of X-rays while simultaneously measuring the kinetic energy and number of electrons that escape from the top 1 to 10 nm of the material being analyzed. XPS requires ultra-high vacuum (UHV) conditions. XPS is a surface chemical analysis technique that can be used to analyze the surface chemistry of a material in its "as received" state, or after some treatment, for example: fracturing, cutting or scraping in air or UHV to expose the bulk chemistry, ion beam etching to clean off some of the surface contamination, exposure to heat to study the changes due to heating, exposure to reactive gases or solutions, exposure to ion beam implant, exposure to ultraviolet light. A typical XPS spectrum is a plot of the number of electrons detected (sometimes per unit time) (Y-axis, ordinate) versus the binding energy of the electrons detected (X-axis, abscissa). Each element produces a characteristic set of XPS peaks at characteristic binding energy values that directly identify each element that exist in or on the surface of the material being analyzed. These characteristic peaks correspond to the electron configuration of the electrons within the atoms, e.g., 1s, 2s, 2p, 3s, etc. The number of detected electrons in each of the characteristic peaks is directly related to the amount of element within the area (volume) irradiated. To generate atomic percentage values, each raw XPS signal must be corrected by dividing its signal intensity (number of electrons detected) by a "relative sensitivity factor" (RSF) and normalized over all of the elements detected. To count the number of electrons at each kinetic energy value, with the minimum of error, XPS must be performed under ultra-high vacuum (UHV) conditions because electron counting detectors in XPS instruments are typically one meter away from the material irradiated with X-rays.

It is important to note that XPS detects only those electrons that have actually escaped into the vacuum of the instrument. The photo-emitted electrons that have escaped into the vacuum of the instrument are those that originated from within the top 10 to 12 nm of the material. All of the deeper photo-emitted electrons, which were generated as the X-rays penetrated 1– 5 micrometers of the material, are either recaptured or trapped in various excited states within the material. For most applications, it is, in effect, a non-destructive technique that measures the surface chemistry of any material. So we measure the bare 6H-SiC and irradiated 6H-SiC during 2 hr. We can verify carbon layer on the irradiated 6H-SiC surface. It is confirmed the Si-C bonding energy (282.8 eV) in the bare 6H-SiC sample and the C-C bonding energy (284.6 eV) in the irradiated 6H-SiC during 2 hr [Fig 2-

10]. Because of Si terminated 6H-SiC, it appears that the quantification of Si and C is 40.68 %, 39.34 % respectively. After e-beam irradiation on 6H-SiC, it changes the quantification to Si = 8.48 %, C = 66.73 % [Table 2-2]. The degrees the C elements are increased up to 1.5 times, whereas Si elements are decreased rapidly. It is found that the e-beam irradiation sublimates elements of Si on the 6H-SiC. And the carbon layer with thin thickness remains on the irradiated 6H-SiC surface.

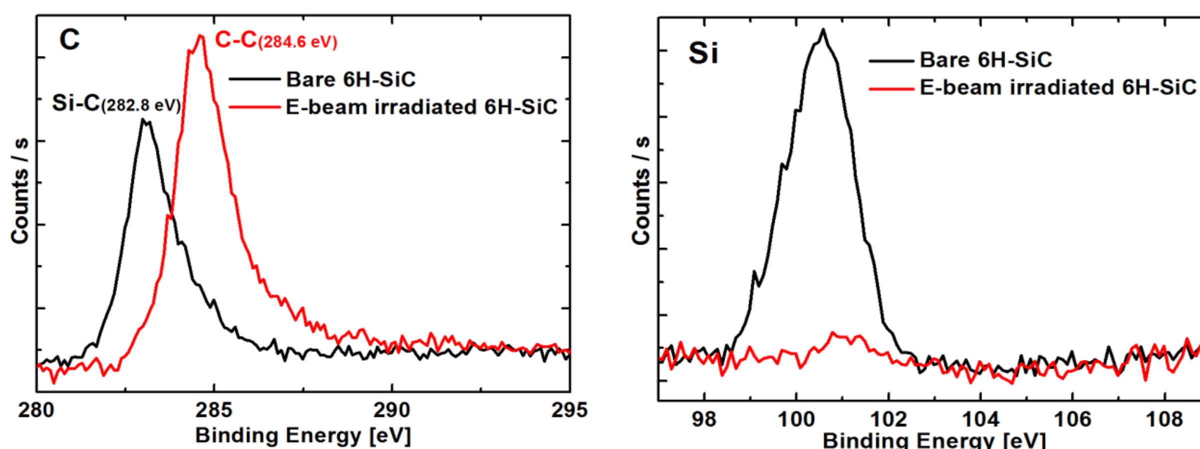

Figure 2-10: XPS spectra of 6H-SiC and graphene layers formed by e-beam irradiation (2 hr). After e-beam irradiation, surface of 6H-SiC changes from Si-C bond (282.8 eV) to C-C bond (284.6 eV) and the XPS peaks of C atoms are increased than bare 6H-SiC peak. The XPS peaks of Si atoms are vanished compared with bare 6H-SiC peak.

	Bare 6H-SiC (At. %)	Irradiated 6H-SiC (At. %)
C	39.34	66.73
Si	40.68	8.48

Table 2-2: XPS elements and quantifications of 6H-SiC and graphene layers form by e-beam irradiation (2 hr). After e-beam irradiation, quantifications of C elements are increased more than 1.5 times and Si elements are decreased considerably than elements of bare 6H-SiC.

2.2.2. Electrical Characteristics

The structural and compositional analysis had been completed, the electrical properties of the formed epitaxial graphene were measured.

2.2.2.1. Two-Terminal Resistance Measurement

To investigate the electrical properties of the formed graphene layers, we measured two-terminal resistance through the graphene layers by making Ni / Au contacts on the irradiated 6H-SiC. The diameter of dot is 50 um and the thicknesses of Ni and Au are 500 nm and 200 nm respectively [Fig. 2-11]. The electrical measurements were done using a semiconductor parameter analyzer (B1500A, Agilent). The electrical properties of sample surface were compared before and after e-beam irradiation during 2 hr. The I-V curve on the bare 6H-SiC shows the typical back-to-back Schottky junction behavior [Fig. 2-12]. Whereas the I-V curve on the irradiated 6H-SiC shows the Ohmic behavior. That is, the electrical characteristics change from semiconductor properties of Schottky junction into metal properties of Ohmic junction by using e-beam irradiation. And it is found that the two-terminal resistance of the irradiated 6H-SiC decreased over ~1000 times than the bare 6H-SiC. This indicates that the top surface of the 6H-SiC substrate changed from semiconducting to metallic by e-beam irradiation, supporting the formation of graphene layers.

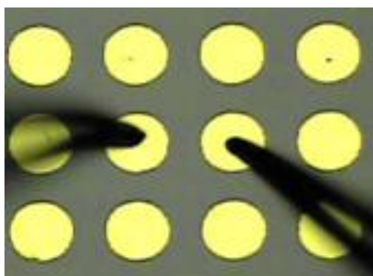

Figure 2-11: Image of dot metal contacts

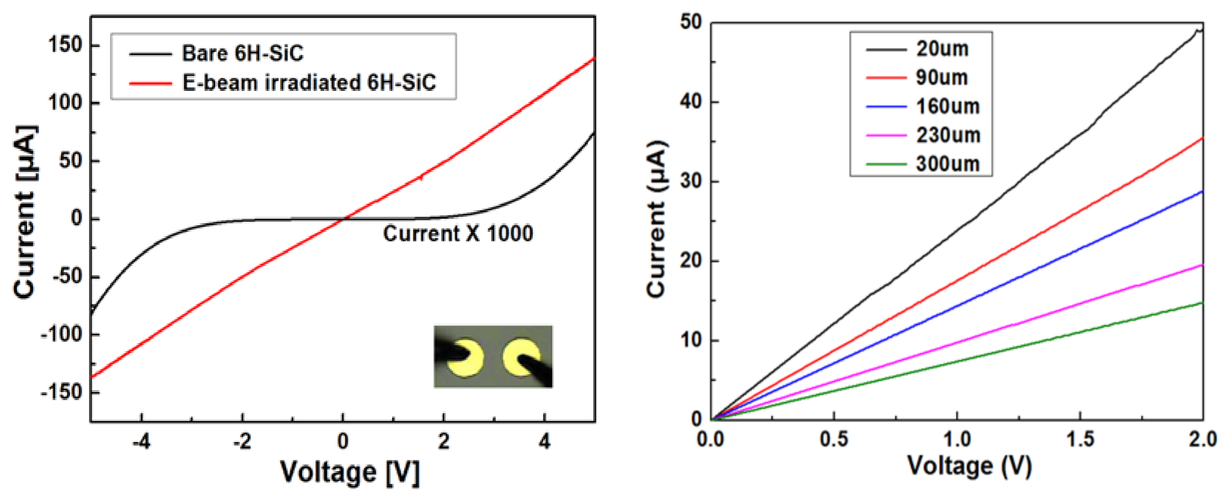

Figure 2-12: The current-voltage characteristics of graphene layers formed by e-beam irradiation (2 hr). The current-voltage curve of bare 6H-SiC and graphene layer form by e-beam irradiation (2 hr). 6H-SiC current × 1000.

2.2.2.2. Circular Transmission Line Model

We make Circular Transmission Line Model (CTLM) to investigate the sheet resistance (R_{sh}) and contact resistance (R_c) of formed graphene layer on the irradiated 6H-SiC. The CTLM structure is commonly used to determine the specific contact resistance of ohmic contact systems in semiconductor devices [61][62]. Requiring just one lithography step, CTLM structure is simple and powerful tool in characterizing the specific contact resistance for devices. Unlike the traditional TLM, the CTLM has the advantage of not requiring a mesa etch. Using a lift-off process realization therefore just takes one lithography step. Using resistance - gap spacing graph, enable to calculate sheet resistance and contact resistance from slope and y-intercept of graph respectively. It is imperative that a semiconductor device can be connected to the outside world with no adverse change to its current-voltage characteristics and no additional voltagedrop. It can be accomplished only through low-resistance ohmic contact on the semiconductor. An ideal ohmic contact is one where, when combined with the semiconductor, no barriers to the carrier flow are encountered in either the positive and negative direction. Ideally, this occurs when the work functions of the semiconductor and the metal are about the same, and there are no appreciable interface states which tend to pin the Fermi Level. However, it is not possible as the work function of the semiconductor varies with doping concentration and for wide bandgap semiconductor such as p-GaN, there is an added difficulty because it is impossible to find a metal that has a large enough workfunction. Hence, it is not an easy task to achieve a good ohmic contact between p-GaN and metal. In order to provide some understanding on ohmic contacts, basic physics of metal-semiconductor contact is briefly discussed in this chapter. In addition, the basic principles of the CTLM, which is used to measure the specific contact resistance are introduced [63]. For a contact between two dissimilar materials, such as metal and semiconductor, there exists a contact resistance, R_c which is a metal- and geometry-dependent parameter as its magnitude is determined by the sheet resistance of the conducting semiconductor, the contact area, and etc. Consequently, contact resistance is not a useful parameter to characterize contacts. Another parameter that is independent on the measurement and geometry of the contact, known as the specific contact resistance, R_c is often used to parameterize the interface. It is defined as the resistance of a unit area of the thin interfacial layer between the bulk metal and semiconductor substrate. Physically, R_c is the finite resistance seen by the infinitesimal current crossing the metal-semiconductor interface that has an infinitesimally small potential difference. As the specific contact resistance rc cannot be measured directly but must be inferred from a measurement on a real contact, hence several approaches have been used to model the current-voltage behavior of the contact and to extract rc from the equations from the measured quantities of current (I) and voltage (V). One of the approaches is CTLM which will be discussed in detail.

In the following section, the basic concepts and principles of CTLM are presented [64]. Test pattern of either circular or rectangular geometry is commonly used to determine the specific contact resistance of ohmic contact systems in semiconductor devices, as depicted in [Fig. 2-13] and [Fig. 2-14]. However, a mesa structure needs to be fabricated if the rectangular test pattern is used, unlike circular test patterns where such complication can be totally avoided. The definition of mesa is required to confine the current flow between two contacts. As a result, circular pattern has been chosen in this work.

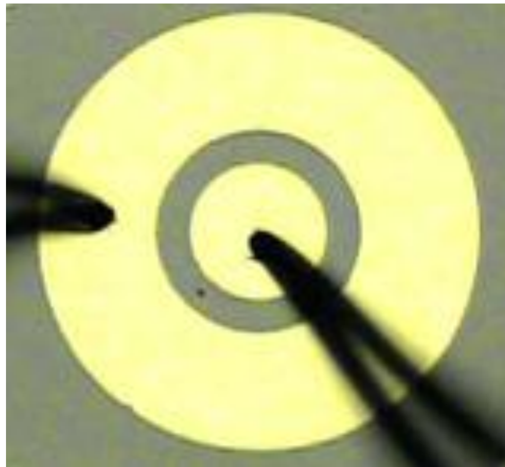

Figure 2-13: CTLM image for metal contact

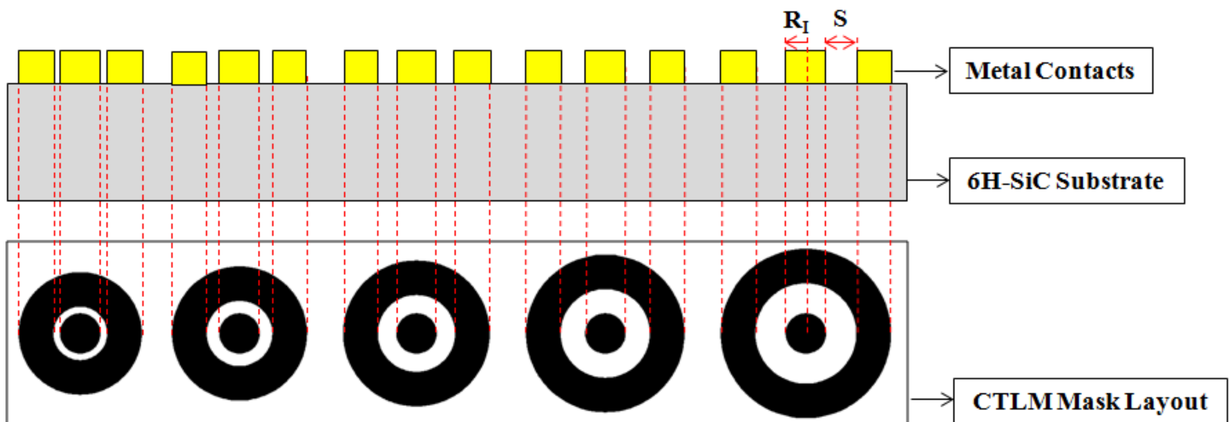

Figure 2-14: Cross-section image of CTLM

By having a constant current through the inner circular and outer contact pads using a Precision Parameter Analyzer, as indicated in [Fig. 2.15], there will be a voltage drop, DV, across the separation d between two points [65][66].

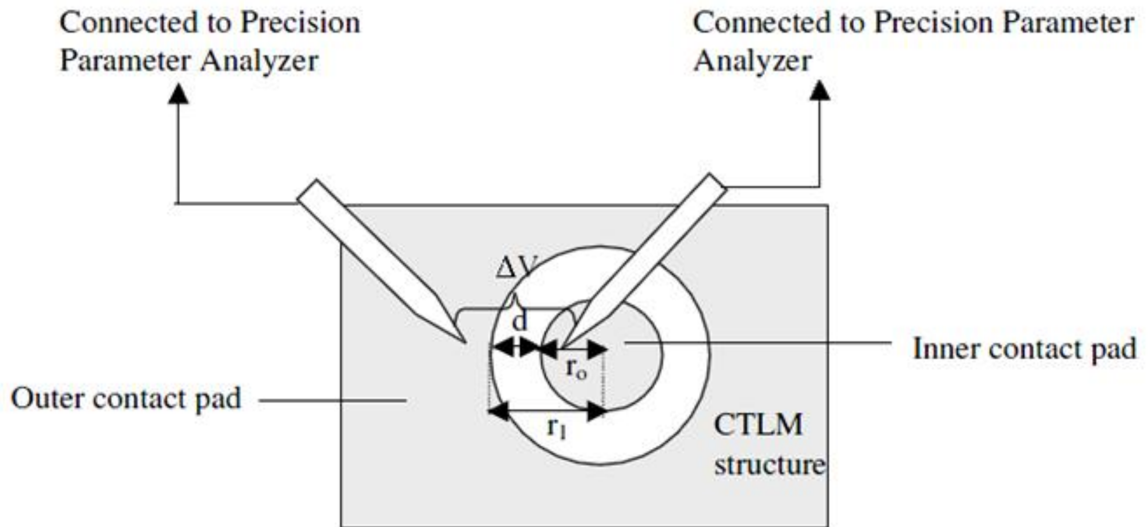

Figure 2-15: Pattern of CTLM

The voltage drop across the separation d, is given by

$$R_T = \frac{R_S}{2\pi}\left\{ ln\left(\frac{R_I + d}{R_I}\right) + L_T\left(\frac{1}{R_I} + \frac{1}{R_I + d}\right)\right\}$$

$$R_T = \frac{R_S}{2\pi R_I}\left(d + 2L_T\right) \qquad since \;\; 2\pi\left(R_I - d\right) >> d$$

R_T = Total resistance

R_S = Semiconductor sheet resistance

L_T = Transfer lengh

R_I = Radius of the inner electrode

d = Spacing between inner and outer contacts

where R_T includes the probe resistance. It can be seen from equation that there is a linear relationship between R_T and the circular contact pad spacing, d. Thus, a graph of R_T versus d can be plotted, where

the slope of the graph gives the value and the interception with the vertical R_T axis gives the value, as shown in [Fig. 2-16].

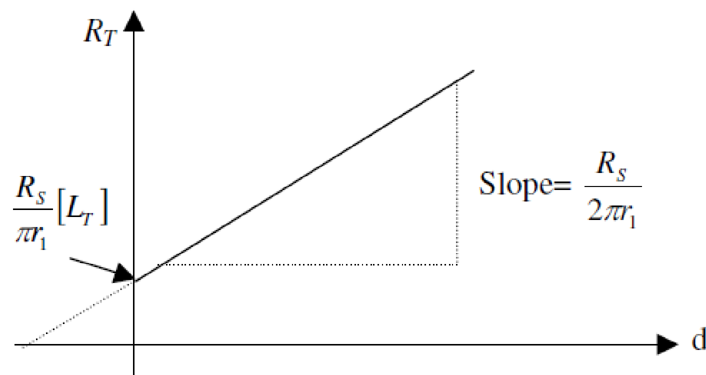

Figure 2-16: Graph of R_T versus d

We manufacture the inner circular contact of diameter of 50 um and varying gap spacing (10~50 um) make the outer circular contact. The contact metals are Ni / Au. The circular patterns are made on the irradiated 6H-SiC by using lithography process. According the patterns, deposit the Ni / Au (500 nm / 200 nm) and execute the lift-off process. The electrical characteristics are measured by the Prove-station from Agilent Technologies, Inc. (B1500A). According to distance of gap spacing, the resistance is measured [Fig 2-17, 2-18].

The figure shows the measured resistances (open squares) between the inner and outer circular contacts as the contact pad spcing changes. The red line is the curve fitted to the measured data with the known equation for CTLM structure. Using the resistance equation of CTLM structure, we calculate the sheet resistance and contact resistance of the irradiated 6H-SiC. About measured values, we obtain linear graph by carrying out linear fitting. So we confirm the following values are obtained : R_{sh} = 6.7 kΩ/□ ; R_C = 0.18 kΩ ; L_T = ~1.8 μm. Then the specific contact resistance at the interface of Ni and epitaxial graphene is calculated to be $\rho_c = R_{sh} L_T$ = ~ 2.2×10^{-7} Ω cm^2. The extracted sheet resistance is relatively high compared with those of the common thermal-annealing-induced of CVD-grown graphene layers. This implies that our epitaxial graphene layers induced by e-beam irradiation might contain more grain boundaries due to smaller grains or less continuous than the graphene layers induced by the other two methods. It needs to improve the quality of formed graphene layers.

And we measure the current-voltage curve with different gap spacing on the irradiated 6H-SiC. the more the distance of gap spacing is decreased at an interval of 10 um, the more the conductivity is increased every 1.5 times.

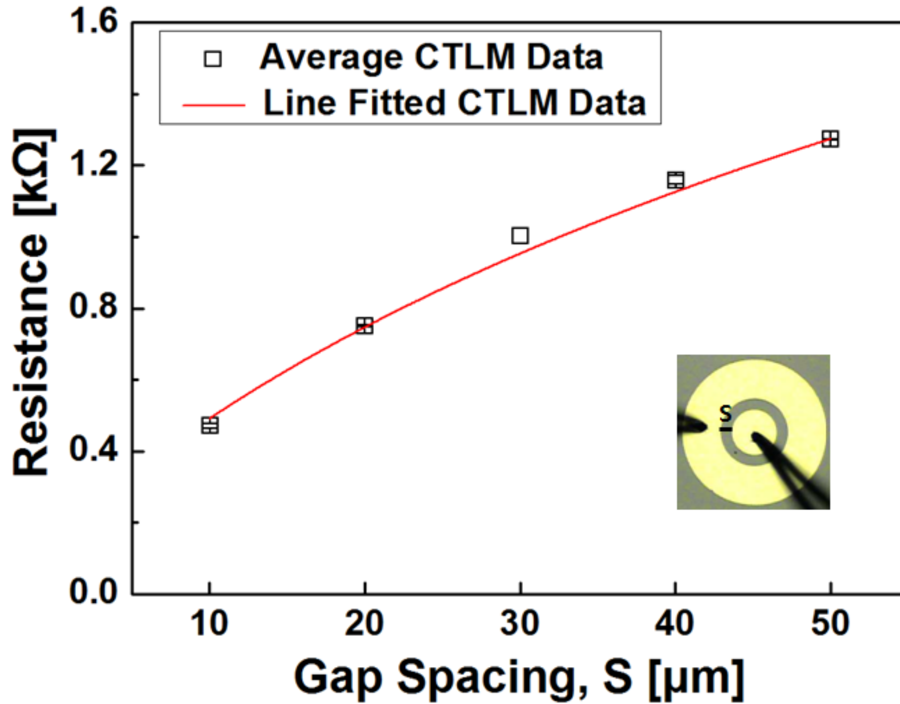

Figure 2-17: R_T versus d curve of CTLM. The measured resistances (open squares) between the inner and outer circular contacts in the CTLM structure with varying contact pad spacing and the curve (red line) fitted to the measured data by using the known equation between resistance and contact pad spacing for the CTLM structure.

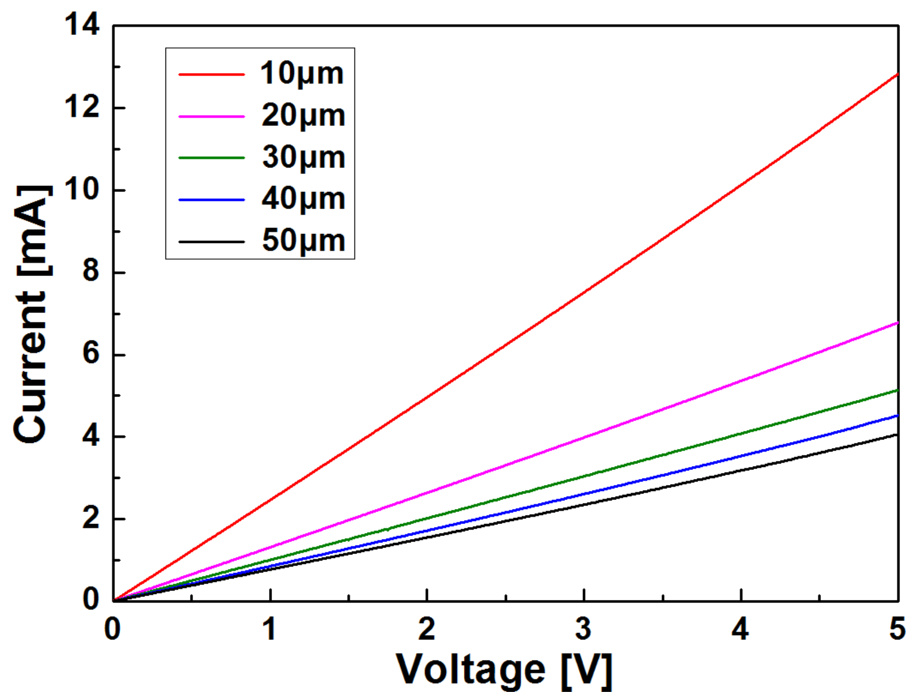

Figure 2-18: Current-voltage curve of CTLM. The IV curve with different gap spacing on graphene layers form by e-beam irradiation.

Chapter III

Summary & Conclusion

The SiC and graphene are the important materials in this research. I explained grow method of graphene layer on SiC substrate.

SiC is used in various fields until now. With the recent technological progress in manufacturing power devices based on wide band gap materials SiC, the operating voltage range, the switching speed and/or specific on-resistance have been and will be improved significantly compared to silicon power devices. In case these new devices are applied in power electronic systems, the improvements on the device level will impact also the system performance, which is usually measured by power density, efficiency, weight, reliability, and costs. In power electronic systems there has been a continuous trend towards a higher system power density in the last decades and due to environmental concerns and rising energy costs, also the efficiency of the systems became important system performance criteria, over the past years besides costs. For meeting these demands, the development of power semiconductors is a crucial enabling factor

Graphene exhibits many outstanding material properties outperforming other semiconductor materials. Especially, its remarkable transport properties make it a prominent candidate for future micro- and nano- electronic applications that can replace the current Si-based technologies. Typically, graphene can be produced by mechanical exfoliation of graphite or epitaxially on SiC and metals. Following the successful isolation of graphene from graphite, there has been an enormous amount of research activities for fabricating high-quality graphene on a large scale. The epitaxial graphene on SiC has an essential benefit in terms of uniform large-scale growth since it can be induced just by heating an entire SiC wafer to high temperature in Ultra High Vacuum or Ar atmosphere.

I performed 8 kV, 2 mA e-beam irradiation on a 6H-SiC with varying fluences and irradiation times by using an e-beam evaporator. The sublimation of Si on a 6H-SiC surface enables the formation of

epitaxial graphene layers to be more easy and controlled. The merit of research is representing relatively easy and controlled process method for grow graphene. And it can lower process temperature than existing method of heating SiC material. The heating SiC material process temperature is over 1300 ℃. But temperature of my study is ~650 ℃.

I verify distinct D, G, and 2D peaks of the graphene layers by using Raman spectrum. And it is found that the Si and O elements are vanished and C element is increased up to about 1.5 times through AES. By XPS measurement, the bond structure of 6H-SiC is changed from Si-C bond to C-C bond by e-beam irradiation. And It is verified that graphene layer's number is 7 ~ 8, a layer's thickness is 0.32 nm.

The current-voltage curve turns into the shape of Ohmic junction from Schottky junction and the conductivity of 6H-SiC is increased more than 1000 times. Finally, to obtain the sheet resistance and contact resistance, I manufacture CTLM structures. The sheet resistance and contact resistance of graphene layer formed by e-beam irradiation are 6.7 kΩ/□ and 0.18 kΩ respectively. This relatively high sheet resistance is believed to be due to small grains or local discontinuity of the formed epitaxial graphene. The experimental results suggests that it would be possible to directly write epitaxial graphene patterns on a SiC substrate without any additional patterning processes involved if a proper equipment capable of focusing e-beam and adjust its location in an arbitrary fashion is developed.

REFERENCES

1. Stephen E. Saddow & Anant Agarwal 2004, *Advances in Silicon Carbide Processing and Applications*, Artech House Publishers, America.

2. G. Brezeanu 2005, 'Silicon Carbide (SiC): A short history. An analytical approach for SiC power device design', *IEEE*, vol. 5, pp. 345-348.

3. Mohit Bhatnagar & B. Jayant Baliga 1993, 'Comparison of 6H-SiC, 3C-SiC, and Si for Power Devices', *IEEE,* vol. 3, pp. 645-655.

4. Jim Richmond, Stuart Hodge & John Palmour 2004, 'Silicon Carbide Power Applications and Device Roadmap', *Power Electronics Europe,* pp. 17-21.

5. S.I. Vlaskina 2002, 'Silicon carbide LED', *Semiconductor Physics, Quantum Electronics & Optoelectronic',* vol. 5, pp. 71-75.

6. Rebecca Cheung 2006, *Silicon Carbide Micro Electromechanical Systems for Harsh Environments,* Imperial College Press, London.

7. Takahiro M, Yoshitake K, Taku Y, Naoki S & Jun A 2008, 'Superconductivity in carrier-doped silicon carbide', *Sci. Technol. Adv. Mater.,* vol 9, pp. 1-8.

8. Philip G. Neudeck 2002, *Homoepitaxial and Heteroepitaxial Growth on Step-Free SiC Mesas,* Brookpark Road, Cleveland.

9. Qingsong H, Xiaolong C, Jun L, Wenjun W, Gang W, Wanyan W, Rong Y, Yu L & Liwei G 2010, 'Epitaxial graphene on 4H-SiC by pulsed electron irradiation', *Chem. Commun.,* vol 46, pp. 4917-4919.

10. Gary L Harris 1995, *Properties of Silicon Carbide,* Inspec Publishers, United Kingdom.

11. Richard M. Laine & Florence Babonneau 1992, 'Preceramic Polymer Routes to Silicon Carbide', *Chem. Mater.,* vol. 5, pp. 260-279.

12. H. Morkoc, S. Strite, G. B. Gao, M. E. Lin, Sverdlov & M. Burns 1993, 'Large-band-gap SiC, III-V nitride, and II-VI ZnSe-based semiconductor device technologies', *J. Appl. Phys.,* vol. 76, pp. 1363-1398.

13. K. B. Park, Y. Ding, J. P. Pelz, P. G. Neudeck & A. J. Trunek 2006, 'Valence band structure and band offset of 3C- and 4H-SiC studied by ballistic hole emission microscopy', *Appl. Phys. Lett.,* vol. 89, pp. 042103.

14. Barry A. A. L. van Setten, Michiel Makkee, & Jacob A. Moulijn 2001, 'Science and Technology of Catalytic Diesel Particulate Filters', *Catalysis Reviews.*, vol. 43, pp. 489-564.

15. F. La Via, F. Roccaforte, A. Makhtari, V. Raineri, P. Musumeci, & L. Calcagno 2002, 'Structural and electrical characterisation of titanium and nickel silicide contacts on silicon carbide', *Microelectronic Engineering,* vol. 60 , pp. 269–282.

16. Hiroshi Ishiwara, Kiyomi Naruke & Seijiro Furukawa 1982, 'Electrical Activation of B Ions Implanted in Deposited-Amorphous Si during Solid Phase Epitaxy', *Japanese Journal of Applied Physics,* vol. 21, pp. L577-L579.

17. Tetsuya T., Shigetoshi S., Maki K., Migo K., Hideo T., Hiroshi A. & Isamu A. 1997, 'Quantum-Confined Stark Effect due to Piezoelectric Fields in GaInN Strained Quantum Wells', *Japanese Journal of Applied Physics,* vol. 36, pp. L382-L385.

18. A. P. Bibilashvili, A. B. Gerasimov, R. E. Kazarov, & Z. D. Samadashvili 1999, 'Catalytic plasma anodization of single-crystal 6H–SiC structures', *Tech. Phys. Lett.*, vol. 25, pp. 593-594.

19. A. K. Geim & K. S. Novoselov 2007, 'The rise of graphene', *Nature Materials,* vol. 6, pp. 183-191.

20. K. S. Novoselov, A. K. Geim, S. V. Morozov, D. Jiang, Y. Zhang, S. V. Dubonos, I. V. Grigorieva & A. A. Firsov 2004, 'Electric Field Effect in Atomically Thin Carbon Films', *Science,* vol. 306, pp. 666-669.

21. Jannik C. Meyer1, A. K. Geim, M. I. Katsnelson, K. S. Novoselov, T. J. Booth & S. Roth 2007, 'The structure of suspended graphene sheets', *Nature,* vol. 446, pp. 60-63.

22. Masa Ishigami, J. H. Chen, W. G. Cullen, M. S. Fuhrer & E. D. Williams 2007, 'Atomic Structure of Graphene on SiO_2', *Nano Lett.,* vol. 7, pp. 1643-1648.

23. Daisuke Kasuya, Masako Yudasaka, Kunimitsu Takahashi, Fumio Kokai & Sumio Iijima 2002, 'Selective Production of Single-Wall Carbon Nanohorn Aggregates and Their Formation Mechanism', *J. Phys. Chem.,* vol. 106, pp. 4947-4951.

24. P. R. Wallace 1946, 'The Band Theory of Graphite', *Physical Review,* vol. 71, pp. 622-634.

25. J. C. Charlier, P. C. Eklund, J. Zhu, A. C. Ferrari 2008, 'Electron and Phonon Properties of Graphene: Their Relationship with Carbon Nanotubes', *Topics Appl. Physics,* vol. 111, pp. 673-709.

26. Gordon W. Semenoff 1984, 'Condensed-Matter Simulation of a Three-Dimensional Anomaly',

Physical Review Letters, vol. 53, pp. 2449-2452.

27. Paul L. McEuen 1998, 'Carbon-based electronics', *Nature,* vol. 393, pp. 15-17.

28. K. S. Novoselov, A. K. Geim, S. V. Morozov, D. Jiang, M. I. Katsnelson, I. V. Grigorieva, S. V. Dubonos & A. A. Firsov 2005, 'Two-dimensional gas of massless Dirac fermions in graphene', *Nature,* vol. 438, pp. 197-200.

29. S.V. Morozov, K. S. Novoselov, M. I. Katsnelson, F. Schedin, D. C. Elias, J. A. Jaszczak & A. K. Geim 2008, 'Giant Intrinsic Carrier Mobilities in Graphene and Its Bilayer', *Physical Review Letters,* vol. 100, pp. 016602.

30. Jian-Hao Chen, Chaum Jang, Shudong Xiao, Masa Ishigami & Michael S. Fuhrer 2008, 'Intrinsic and extrinsic performance limits of graphene devices on SiO2', *Nature Nanotechnology,* vol. 3, pp. 206-209.

31. Akin Akturk & Neil Goldsman 2008, 'Electron transport and full-band electron-phonon interactions in graphene', *J. Appl. Physics,* vol. 3, pp. 053702.

32. J. H. Chen, C. Jang, S. Adam, M. S. Fuhrer, E. D. Williams & M. Ishigami 2008, 'Charged-impurity scattering in graphene' , *Nature Physics,* vol. 4, pp. 377-381.

33. Shaffique Adam, E. H. Hwang, V. M. Galitski & S. Das Sarma 2007, 'A self-consistent theory for graphene transport', *PNAS,* vol. 104, pp. 18392-18397.

34. Jiannis K. Pachos 2008, 'Manifestations of topological effects in graphene', *Contemporary Physics*, vol. 20, pp. 115-120.

35. R. R. Nair, P. Blake, A. N. Grigorenko, K. S. Novoselov, T. J. Booth, T. Stauber, N. M. R. Peres & A. K. Geim 2008, 'Fine Structure Constant Defines Visual Transparency of Graphene', *Science,* vol. 320, pp. 1308.

36. Yuanbo Zhang, Tsung-Ta Tang, Caglar Girit, Zhao Hao, Michael C. Martin, Alex Zettl, Michael F. Crommie, Y. Ron Shen & Feng Wang 2009, 'Direct observation of a widely tunable bandgap in bilayer graphene', *Nature,* vol. 459, pp. 820-822.

37. Junfeng Liu, A. R. Wright, Chao Zhang & Zhongshui Ma 2008, 'Strong terahertz conductance of graphene nanoribbons under a magnetic field', *Appl. Phys. Lett.,* vol. 93, pp. 041106.

38. Ulas Kürüm, Okan Ö ner Ekiz, H. Gul Yaglioglu, Ayhan Elmali & Mustafa Ü rel 2011, 'Electrochemically tunable ultrafast optical response of graphene oxide', *Appl. Phys. Lett.,* vol. 98, pp. 141103.

39. Hongki Min, Bhagawan Sahu, Sanjay K. Banerjee & A. H. MacDonald 2007, '*Ab initio* theory of gate induced gaps in graphene bilayers', *Physical Review,* vol. 75, pp. 155115.

40. Lola Brown, Robert Hovden, Pinshane Huang, Michal Wojcik, David A. Muller & Jiwoong Park 2012, 'Twinning and Twisting of Tri- and Bilayer Graphene', *Nano Lett.,* vol. 12, pp. 1609-1615.

41. Andrey K. Geim & Allan H. Macdonald 2007, *Graphene: Exploring carbon flatland*, Physics Today, America.

42. C. Riedl, C. Coletti, T. Iwasaki, A. A. Zakharov & U. Starke 2009, 'Quasi-Free-Standing Epitaxial Graphene on SiC Obtained by Hydrogen Intercalation', *Physical Review Lett.,* vol. 103, pp. 246804.

43. Peter Sutter 2009, 'How silicon leaves the scene', *Nature Materials,* vol. 8, pp. 171-172.

44. Taisuke Ohta, Aaron Bostwick, J. L. McChesney, Thomas Seyller, Karsten Horn, & Eli Rotenberg 2007, 'Interlayer Interaction and Electronic Screening in Multilayer Graphene Investigated with Angle-Resolved Photoemission Spectroscopy', *Physical Review Lett.,* vol. 98, pp. 206802.

45. J. S. Moon, D. Curtis, M. Hu, D. Wong, C. McGuire, P. M. Campbell, G. Jernigan, J. L. Tedesco, B. VanMil, R. Myers-Ward, C. Eddy, Jr., & D. K. Gaskill 2009, 'Epitaxial-Graphene RF Field-Effect Transistors on Si-Face 6H-SiC Substrates', *IEEE,* vol. 30, pp. 650-652.

46. I. Pletikosic, M. Kralj, P. Pervan, R. Brako, J. Coraux, A. T. N'Diaye, C. Busse & T. Michely 2009, 'Dirac Cones and Minigaps for Graphene on Ir(111)', *Physical Review Lett.,* vol. 102, pp. 056808.

47. Sukang B, Hyeongkeun K, Youngbin L, Xiangfan Xu, Jan-Sung Park, Yi Z. & Sumio Iijima 2010, 'Roll-to-roll production of 30-inch graphene films for transparent electrodes', *Nature Nanotechnology,* vol. 20, pp. 101038.

48. Keun Soo Kim, Yue Zhao, Houk Jang, Sang Yoon Lee, Jong Min Kim, Kwang S. Kim, Jong-Hyun Ahn, Philip Kim, Jae-Young Choi & Byung Hee Hong 2009, 'Large-scale pattern growth of graphene films for stretchable transparent electrodes', *Nature,* vol. 457, pp. 706-709.

49. Ram Sevak Singh, Venkatram Nalla, Wei Chen, Andrew Thye Shen Wee & Wei Ji 2011, 'Laser Patterning of Epitaxial Graphene for Schottky Junction Photodetectors', *ACSNANO,* vol. 5, pp. 5969-5975.

50. M. Zacharias & P.M. Fauchet 1998, 'Light emission from Ge and GeO_2 nanocrystals', *Journal of*

Non-Crystalline Solids, vol. 227, pp. 1058-1062.

51. Zachary J. Smith and Andrew J. Berger 2008, 'Integrated Raman- and angular-scattering microscopy', *Optics Lett.,* vol. 33, pp. 714-716.

52. Katrin Kneipp, Harald Kneipp, Irving Itzkan, Ramachandra R. Dasari & Michael S. Feld 1999, 'Surface-enhanced non-linear Raman scattering at the single-molecule level', *Chemical Physics,* vol. 247, pp. 155-162.

53. Bettina Voutou & Eleni-Chrysanthi Stefanaki 2008, *Electron Microscopy: The Basics,* Physics of Advanced Materials Winter School, Greece.

54. Michael J. Dykstra & Laura E. Reuss 2003, *Biological Electron Microscopy,* Springer, America.

55. Wubeshet Sahle & Ildiko Laszlo 1995, 'Airborne inorganic fibre level monitoring by Transmission Electron Microscope (TEM): Comparison of direct and indirect sample transfer methods', *Ann. Occup. Hyg.,* vol. 40, pp. 29-44.

56. A. Wucher 1996, *Surface and Thin Film Analysis with Electron and Mass Spectrometric Techniques,* Kaiserslautern, America.

57. D. Briggs & John T. Grant 2003, *Surface Analysis by Auger and x-Ray Photoelectron Spectroscopy,* IM publisher, America.

58. D. Briggs & M. P. Seah 1996, *Practical Surface Analysis, Auger and X-ray Photoelectron Spectroscop',* Paperback, America.

59. K. Siegbahn & K. Edvarson 1955, *Spectroscopy in the precision range,* Nuclear Physic, Sweden.

60. D. W. Turner & M. I. Al Jobory 1962, 'Determination of Ionization Potentials by Photoelectron Energy Measurement', *J. Chem. Phys.* vol. 37, pp. 3007-3008.

61. Dieter K. Schroder 2006, *Physics of Metal-Semiconductor Contact and Circular Transmission Line Model (CTLM),* John Wiley & Sons, Inc., Canada.

62. Dieter K. Schroder 2006, *Contact Resistance and Schottky Barriers,* John Wiley & Sons, Inc., Canada.

63. Dieter K. Schroder 2006, *Semiconductor Material and Device Characterization, Third Edition,* John Wiley & Sons, Inc., Canada.

64. J.H. Klootwijk, C.E. Timmering 2004, 'Merits and Limitations of Circular TLM structures for contact resistance determination for novel 111-V HBTs', *IEEE,* vol. 17, pp. 247-252.

65. G. K. Reeves & H. B. Harrison 1982, ‘Obtaining the Specific Contact Resistance from Transmission Line Model Measurements’, *IEEE,* vol. EDL-3, pp. 111-113.

66. Gregory S. Marlow & Mukunda B. Das 1982, ‘The effects of contact size and non-zero metal resistance on the determination of specific contact resistance’, *Solid-State Electronics,* vol. 25, pp. 91-94.

Acknowledgement

I owe the deepest gratitude to my supervisor, Prof. Kibog Park. His encouragement, inspiration, guidance and support enabled me to develop an understanding of the research. I feel very lucky to be under the direction of Prof. Kibog Park at UNIST.

I want to express my gratitude to Prof. Min Sup Hur and Prof. Kyung Rok Kim for giving me advice about my research as a committee and Prof. Soon-Yong Kwon for cheering me up with sincere words.

I would like to thank my lab members, EMDL people. I am grateful to Young Eun Jeon, Han Byul Jin, Sungchul Jung, Hun Han Yoon and Gahyun Choi. They gave me a valuable advice and encouragement. I acknowledge many people who help me every time I asked them.

Lastly, I really appreciate my parents giving me the most valuable affection to study so far.